NICER uncovers the transient nature of the type-B quasi-periodic oscillation in the black hole candidate MAXI J1348−630

L. Zhang[1],[⋆] D. Altamirano[1], P. Uttley[2], F. García[3], M. Méndez[3], J. Homan[4,5],
J. F. Steiner[6], K. Alabarta[1,3], D. J. K. Buisson[1], R. A. Remillard[7],
K. C. Gendreau[8], Z. Arzoumanian[8], C. Markwardt[8], T. E. Strohmayer[8],
J. Neilsen[9] and A. Basak[2]

[1]*Physics and Astronomy, University of Southampton, Southampton, Hampshire SO17 1BJ, UK*
[2]*Anton Pannekoek Institute for Astronomy, University of Amsterdam, Science Park 904, 1098 XH Amsterdam, The Netherlands*
[3]*Kapteyn Astronomical Institute, University of Groningen, PO Box 800, NL-9700 AV Groningen, the Netherlands*
[4]*Eureka Scientific, Inc., 2452 Delmer Street, Oakland, CA 94602, USA*
[5]*SRON, Netherlands Institute for Space Research, Sorbonnelaan 2, 3584 CA Utrecht, The Netherlands*
[6]*Harvard-Smithsonian Center for Astrophysics, 60 Garden St., Cambridge, MA 02138, USA*
[7]*MIT Kavli Institute for Astrophysics and Space Research, MIT, 70 Vassar Street, Cambridge, MA 02139, USA*
[8]*Astrophysics Science Division, NASA Goddard Space Flight Center, Greenbelt, MD 20771, USA*
[9]*Villanova University, Villanova, PA 19085, USA*

ABSTRACT

We present a systematic spectral-timing analysis of a fast appearance/disappearance of a type-B quasi-periodic oscillation (QPO), observed in four *NICER* observations of MAXI J1348−630. By comparing the spectra of the period with and without the type-B QPO, we found that the main difference appears at energy bands above ∼2 keV, suggesting that the QPO emission is dominated by the hard Comptonised component. During the transition, a change in the relative contribution of the disk and Comptonised emission was observed. The disk flux decreased while the Comptonised flux increased from non-QPO to type-B QPO. However, the total flux did not change too much in the *NICER* band. Our results reveal that the type-B QPO is associated with a redistribution of accretion power between the disk and Comptonised emission. When the type-B QPO appears, more accretion power is dissipated into the Comptonised region than in the disk. Our spectral fits give a hint that the increased Comptonised emission may come from an additional component that is related to the base of the jet.

Key words: accretion, accretion disks – black hole physics – X-rays: binaries – X-ray: individual (MAXI J1348−630)

1 INTRODUCTION

Black hole binaries (BHBs), consisting of a stellar-mass black hole accreting material from a companion star, are typically transient systems. They spend most of their time in a long quiescent period ($L_X \approx 10^{30} - 10^{34}$ erg s^{-1}), and occasionally exhibit bright outbursts during which their X-ray luminosity increases by several orders of magnitude (typically reaching $L_X \approx 10^{37} - 10^{38}$ erg s^{-1}). BHBs in outbursts are characterized by rapid evolution of their X-ray spectral and timing properties, which can be studied in terms of different states (see Homan & Belloni 2005; Remillard & McClintock 2006 for different classification schemes of black hole states). Two main canonical states are usually identified: the

hard state (HS), where the spectrum is dominated by a hard Comptonised component, and the soft state (SS), where the X-ray emission is dominated by a thermal disk component. During the transition between the HS and SS, two additional short-lived states, namely the hard-intermediate state (HIMS) and the soft-intermediate state (SIMS), have been recognized (see Belloni & Motta 2016 for a recent review).

A distinctive timing characteristic of BHBs is the evolution of the low-frequency QPOs with spectral states (see Ingram & Motta 2019 for a recent review of different types of QPOs). As a source evolves from the bright end of the HS to the HIMS, type-C QPOs (up to 20 per cent rms in the 2–60 keV, the full energy band of the Proportional Counter Array aboard the Rossi X-ray Timing Explorer, hereafter *RXTE*/PCA) always appear in the power density spectra (PDS), superimposed on a strong band-limited noise component.

⋆ E-mail: liang.zhang@soton.ac.uk

Their frequency is tightly correlated with spectral changes, moving from a few mHz to 10 Hz as the spectrum softens. Type-C QPOs are thought to have a geometric origin (e.g., Motta et al. 2015; van den Eijnden et al. 2017; Ma et al. 2021), and have been widely explained by Lense-Thirring precession of the hot inner flow (e.g., Schnittman et al. 2006; Ingram et al. 2009). Type-B and type-A QPOs are normally detected in the SIMS, at a similar frequency range (typically 4–8 Hz). Both types are associated with weak broadband noise. Type-B QPOs are relatively strong (up to 5 per cent rms in the *RXTE*/PCA band) and narrow, whereas type-A QPOs are weak (few per cent rms in the *RXTE*/PCA band) and broad features. The physical origin of these two types of QPOs is less clear. Hints of a connection between the appearance of type-B QPO and the launch of discrete jet ejection have been found in several BHBs (e.g., Soleri et al. 2008; Fender et al. 2009; Russell et al. 2019a; Homan et al. 2020; Russell et al. 2020), pointing to a jet-based origin of type-B QPOs. In this work, we will focus our study on the type-B QPOs.

QPOs are typically transient, appearing or disappearing on timescales of a few tens of seconds. Such transient behaviour has been observed in all type-A (Sriram et al. 2021), -B (e.g., Miyamoto et al. 1991; Nespoli et al. 2003; Casella et al. 2004; Huang et al. 2018; Sriram et al. 2021), and -C (Xu et al. 2019; Jithesh et al. 2019; Sriram et al. 2021) QPOs. In particular, fast transitions between different types of low-frequency QPOs or broadband noise components are sometimes observed with significant changes of the source spectrum (e.g., Miyamoto et al. 1991; Takizawa et al. 1997; Wijnands et al. 2001; Homan et al. 2001; Casella et al. 2004; Motta et al. 2011; Sriram et al. 2012, 2013, 2016, 2021). The spectral-timing study of these fast transitions not only provides important evidence on the physical origin of different types of QPOs, but also helps us better understand the mechanism responsible for the state transitions.

Fast QPO transitions were first discovered in *Ginga* data, in GX 339−4 (Miyamoto et al. 1991) and GS 1124−68 (Takizawa et al. 1997) in those observations showing "flip-flop" variations. A 6-Hz type-B QPO, which was visible when the source flux is high, disappeared when the source moved to a low-flux epoch. The transition from the low-flux to high-flux epoch was mainly due to a change in the Comptonised component (Miyamoto et al. 1991). Later with *RXTE*, fast transitions between type-B QPOs and type-A QPOs have been observed in a few BHBs, e.g, GX 339−4 (Nespoli et al. 2003; Motta et al. 2011), XTE J1817−330 (Sriram et al. 2012), XTE J1550−564 (Homan et al. 2001; Sriram et al. 2016) and XTE J1859+226 (Casella et al. 2004; Sriram et al. 2013). Type-C to type-B transitions or vice versa are more frequently seen when the source evolves from the HIMS to the SIMS (e.g., Motta et al. 2011; Homan et al. 2020; Sriram et al. 2021) or from the SIMS back to the HIMS. Direct transitions between type-C QPOs and type-A QPOs were recently found in Swift J1658.2−4242 during the flip-flop variations (Bogensberger et al. 2020).

MAXI J1348−630 is a bright (above 3 Crab at the outburst peak) X-ray transient discovered by *MAXI*/GSC on 2019 January 26 (Yatabe et al. 2019; Tominaga et al. 2020). Following observations of *Swift*/XRT obtained a precise source position (Kennea & Negoro 2019) and confirmed the optical counterpart identified by Denisenko et al. (2019). Observations of the Australia Telescope Compact Array (ATCA) detected a radio counterpart consistent with the X-ray position (Russell et al. 2019b). Based on a spectral-timing analysis of observations from the *Neutron Star Interior Composition Explorer* (*NICER*, Gendreau et al. 2016), Zhang et al. (2020b, hereafter Paper-I) concluded that MAXI J1348−630 is a black hole candidate in a binary system. The source underwent
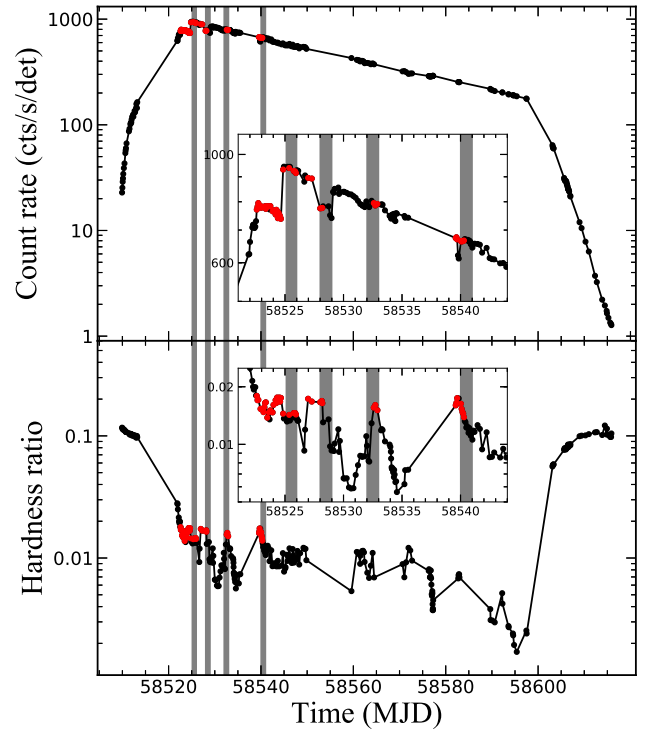

Figure 1. Long-term evolution of the main outburst of MAXI J1348−630. Upper panel: *NICER* 0.5–12 keV light curve. Lower panel: time evolution of the hardness ratio (6–12 keV/2–3.5 keV). Each data point represents the average of a single ISS-orbit dwell. The light curves were normalised by the number of active detectors. The red points correspond to the orbits where a type-B QPO is present. The grey bands mark the four observations in which a fast appearance/disappearance of a type-B QPO was observed. The inset panels show a magnification of the region containing the fast transitions.

an initial full outburst which showed all canonical spectral states of BHBs. After the main outburst, it re-brightened a few times while staying in the HS (Negoro et al. 2019; Zhang et al. 2020b,c; Tominaga et al. 2020). Tominaga et al. (2020) reported the outburst evolution of MAXI J1348−630 as observed with *MAXI*. They noted that the source is in the direction of the Galactic Scutum-Centaurus arm, and due to the low column density it may lie in front of the arm at about 3–4 kpc. Chauhan et al. (2020) determined the distance of MAXI J1348−630 to be $2.2^{+0.5}_{-0.6}$ kpc using H I absorption. Carotenuto et al. (2021) reported the radio monitoring of MAXI J1348−630 with MeerKAT and ATCA. They detected the rise, quenching, and re-activation of the compact jet, as well as two single-sided discrete ejections during the main outburst. Different types of low-frequency QPOs have been observed at different phases of the outburst (see Paper-I for details). Type-B QPOs were detected in the SIMS at a stable frequency of ∼4.5 Hz. Belloni et al. (2020) studied the energy dependence of the fractional rms and phase lags of the type-B QPO using *NICER* data, and García et al. (2021) successfully fitted them simultaneously with a two-component Comptonisation model. Jithesh et al. (2021) studied the energy dependence of the fractional rms of a type-C QPO using simultaneous *AstroSat* and *NICER* observations. They found that the rms of the QPO fundamental is nearly energy independent, while the rms of the subharmonic decreases with energy.

In this work, we present a systematic spectral-timing analysis of the fast appearance/disappearance of a type-B QPO, observed in

Table 1. Log of the four *NICER* observations in which a fast appearance/disappearance of a type-B QPO was observed. The last column lists the exposure time after data filtering and cleaning. The number in parentheses lists the exposure time of the period with a type-B QPO.

Case	ObsId	Start time	Exposure (s)
#1	1200530110	2019 Feb 11 02:17:13	6916 (2944)
#2	1200530113	2019 Feb 13 23:54:20	3089 (601)
#3	1200530117	2019 Feb 18 00:08:00	3558 (1956)
#4	1200530125	2019 Feb 26 00:41:12	11421 (2715)

four *NICER* observations of MAXI J1348−630. The main purpose of this work is to investigate the transient nature and the physical origin of the type-B QPO.

2 OBSERVATIONS AND DATA ANALYSIS

NICER is a soft X-ray telescope onboard the International Space Station (ISS) launched in 2017 June. It provides high throughput in the 0.2–12 keV energy band with an absolute timing precision of ∼100 ns, making it an ideal instrument to study fast X-ray variability. *NICER* consists of 56 co-aligned concentrator X-ray optics, each paired with a single-pixel silicon drift detector. Presently, 52 detectors are active with a peak effective area of ∼1900 cm^2 at 1.5 keV. In our analysis, we excluded data from detectors #14 and #34 as they occasionally show episodes of increased instrumental noise.

NICER has extensively monitored the outburst of MAXI J1348−630 in great detail since its discovery. All observations were reprocessed using the *NICER* software tools NICERDAS version 6.0, distributed with HEASOFT version 6.26. The data reduction procedure was the same as described in Paper-I. To follow the outburst evolution (excluding reflares, see fig. 1 in Paper-I), we extracted net light curves in the 0.5–12 keV energy band as well as the 2–3.5 keV and 6–12 keV energy bands using XSELECT. In the upper panel of Fig. 1 we show the 0.5–12 keV light curve, and in the lower panel we show the evolution of the hardness ratio (6–12 keV/2–3.5 keV) during the main outburst. Individual *NICER* observations are subdivided by continuous data segments, typically separated by several ksec gaps due to the orbit of the ISS. In Fig. 1, each data point represents the average from a single ISS orbit (we define an orbit as a continuous data segment with a net exposure time of longer than 60 s of good time). During the brightest phase of the outburst, some of the detectors were switched off to prevent telemetry saturation and accommodate the high source flux. Therefore, we have normalised the intensity by the number of active detectors in all figures of this paper.

In Paper-I, we produced a PDS in the 0.5–12 keV energy band for each orbit. After the source entered the SIMS, a significant type-B QPO was observed in a number of orbits (see Paper-I and Belloni et al. 2020 for details). In Fig. 1, the orbits containing a type-B QPO are marked in red. The type-B QPO appears in a narrow hardness range, and always corresponds to local peaks in hardness ratio. Upon inspection, we found that the type-B QPOs are not present all the time during the SIMS, and they sometimes switch on/off between orbits. Table 1 lists the log of the four observations in which we found a fast transition. The time intervals of these transitions are marked with grey shaded areas in Fig. 1. In the remaining of the paper, we will focus our analysis on the characteristics of these four observations.

2.1 Timing and spectral analysis

For each of the four observations, we produced a light curve with 5-s binning in the 0.5–12 keV energy band. To calculate the hardness ratio, we also extracted light curves in the 3–12 keV and 0.5–3 keV energy bands. The light curves were not background-subtracted since the background contribution (about 2 counts s^{-1}) is negligible during the brightest phase of the outburst.

PDS shown in this paper were calculated in the 0.5–12 keV energy band with 16-s long intervals and 1/8192-s time resolution (16^{-1} – 4096 Hz frequency range). The resulting PDS were averaged and then normalized in units of (rms/mean)^2 Hz^{-1} (Belloni & Hasinger 1990). The contribution due to Poisson noise was subtracted. We fitted the PDS with a model consisting of a sum of Lorentzian functions.

For the spectral analysis, we extracted background-subtracted spectra using the *NICER* Background Estimator Tool "nibackgen3C50"[1]. The spectra were corrected for the oversampling and rebinned to have at least 30 counts per bin. As suggested by the *NICER* team (private communication), we added a systematic error of 3% below 1.5 keV and 0.5% above 1.5 keV using GRPPHA. We fitted the spectra in the 0.6–10 keV band using XSPEC version 12.10.1. We used the latest calibration files obtained from the CALDB version 20200722, downloaded from NASA's High Energy Astrophysics Science Archive Research Center (HEASARC).

3 RESULTS

3.1 Detailed look at the fast transitions

3.1.1 Light curve and hardness ratio

In Fig. 2, we show the 0.5–12 keV light curve and the evolution of the hardness ratio (3–12 keV/0.5–3 keV) with 5-s binning for the four observations in which a fast appearance/disappearance of a type-B QPO was observed. Obs. #2 contains a total of 7 orbits. We only show the results of the first four orbits in this work, as orbit 5 was taken near half day later than orbit 4 and no QPOs were detected in the remaining three orbits. During the last three orbits, the average count rate decreased from 884 ± 7 to 836 ± 7 counts s^{-1} det^{-1}. The hardness ratio decreased from 0.105 to 0.090. In the case of Obs. #4, a total of 15 orbits were performed in this observation. We ignored the last six orbits without any QPOs. The average count rate decreased slightly from 664 ± 5 to 656 ± 5 counts s^{-1} det^{-1} during the last six orbits. The hardness ratio remained at around 0.090. As we show in section 3.1.2 below, the type-B QPOs were only detected in certain orbits. In Fig. 2 we mark the orbits with the QPO with red, while the ones without the QPO with black. We found the following:

- the turn-on of the type-B QPO does not appear to depend on the 0.5–12 keV count rate as we found QPOs in orbits at higher and lower averaged count rate than those without a significant QPO (see, e.g., Obs #1 and #3);
- within each observation, the orbits with the type-B QPO always correspond to a higher hardness ratio than those without the QPO;
- the hardness value corresponding to the transition changes between observations, possibly decreasing with decreasing count rate.

---

[1] https://heasarc.gsfc.nasa.gov/docs/nicer/tools/nicer_bkg_est_tools.html
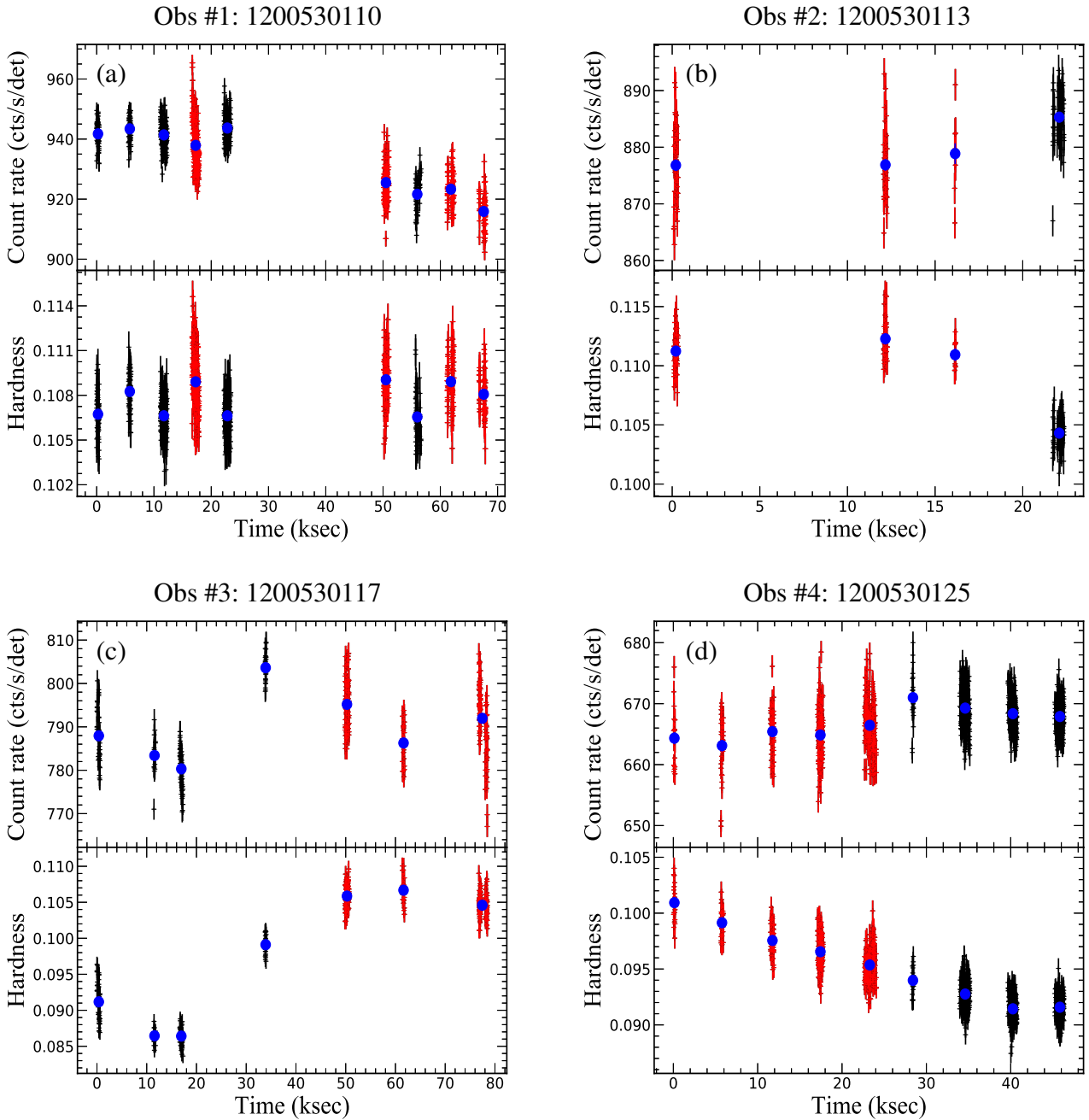
Figure 2. *NICER* 0.5–12 keV light curve and hardness ratio (3–12 keV/0.5–3 keV) with 5-s binning for the four observations in which a fast transition of a type-B QPO was observed. The light curves were normalised by the number of active detectors. The red (black) points represent the orbits with (without) a type-B QPO. The blue points are the average of a single orbit.

3.1.2 *Dynamical and average power spectra*

In Fig. 3 we show the 0.5–12 keV light curve and corresponding dynamical PDS (with a time resolution of 16 s) for each of the four observations shown in Fig. 2. All time gaps were removed and marked with dotted lines. The *x*-axis label is the index of each 16-s PDS. The dynamical PDS reveals that a significant transient QPO around 4 Hz was detected in each observation. In Obs. #1, the QPO was visible in orbits 4, 6, 8 and 9, and disappeared in the other orbits. In Obs. #2 and #4, the QPO was only seen in the first three and five orbits, respectively. While in Obs. #3, the QPO was undetectable in

the first four orbits, but appeared in the last three orbits. In all cases, the frequency of the QPO remained more or less constant within each observation.

Since the dynamical PDS shows that the QPO frequency is stable, we made an average PDS per observation from all the orbits with and without the QPO, respectively. The resulting PDS are shown in Fig. 4 and the best-fitting parameters of the QPO are listed in Table 2. Hereafter we refer to the period with and without the QPO as the BQ (type-B QPO) and NQ (non-QPO) epoch for convenience. The average PDS of epoch BQ shows a primary peak at around 4.3 Hz and its harmonic at around 8.6 Hz. The fundamental of the QPO
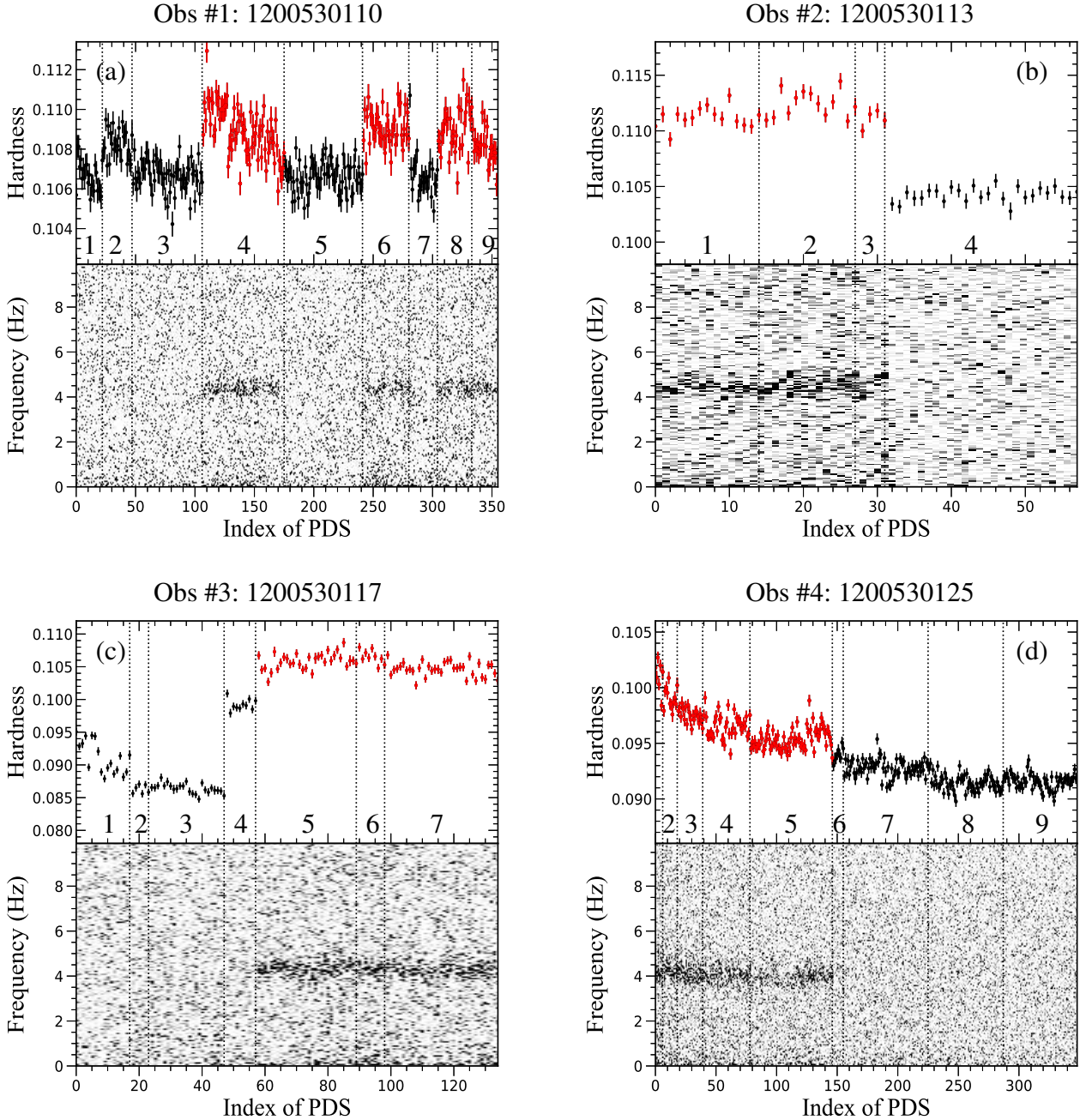
Figure 3. *NICER* hardness ratio (3–12 keV/0.5–3 keV) and corresponding dynamical power spectra with a time resolution of 16 s. All time gaps were removed and marked with dotted lines. The *x*-axis represents the index of each 16-s PDS. The red (black) points represent the period with (without) a type-B QPO. For the dynamical power spectra, the powers were not rms-normalised and Poisson noise was not subtracted. Darker shades correspond to stronger variability.

is very sharp ($Q \approx 6 - 8$) with a fractional rms of $\lesssim 1.6\%$ in the 0.5–12 keV energy band, and ~4–6% in the 3–12 keV energy band. The value of the 3–12 keV fractional rms is consistent with the typical value measured with *RXTE*/PCA at a similar energy band (see, e.g., Casella et al. 2004; Motta 2016). The lower fractional rms amplitude in the 0.5–12 keV energy band is likely due to dilution of the amplitude caused by the non-modulated photons from the disk component. The second-harmonic peak was weak but significantly (>3σ) detected in the average PDS. The frequency of the QPO and its second harmonic does not change much between observations (see Table 2). In addition to the QPO, we detected weak broadband

noise with an integrated fractional rms of ~1–2% in the 0.1–20 Hz frequency range (0.5–12 keV). Based on the properties of the QPO and noise, we can easily identify it as a type-B one (see, e.g., Motta 2016, and references therein). We also investigated the energy dependence of the QPO properties. In Fig. 5 we show the frequency, Q factor, and fractional rms of the QPO observed in Obs. #3, as a function of photon energy. The QPO properties are similar in the other three cases. The frequency and Q factor of the QPO do not change significantly with photon energy. The energy dependence of the fractional rms of the QPO is consistent with Belloni et al.
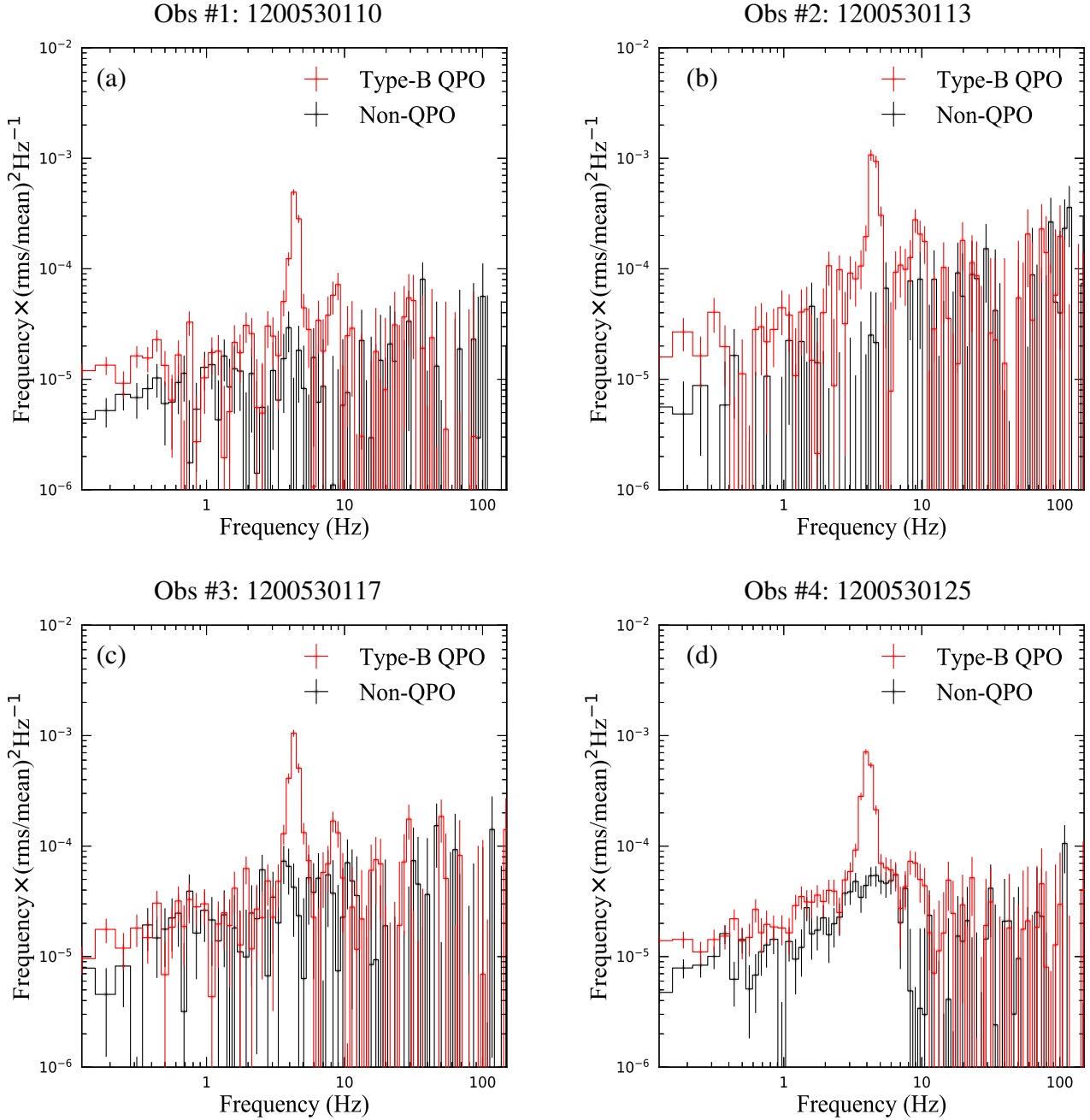
Obs #1: 1200530110

Obs #2: 1200530113

Obs #3: 1200530117

Obs #4: 1200530125

Figure 4. Power spectra averaged from the period with (red) and without (black) a type-B QPO. The average PDS were calculated in the 0.5–12 keV energy band, and rms-normalised (Belloni & Hasinger 1990). The contribution due to Poisson noise was subtracted.

Table 2. Properties of the type-B QPOs for the four observations in which a fast appearance/disappearance of a type-B QPO was observed. The fractional rms of the QPO was calculated in the 0.5–12 keV energy band. The second and third columns list the total count rate and the number of active detectors, respectively.

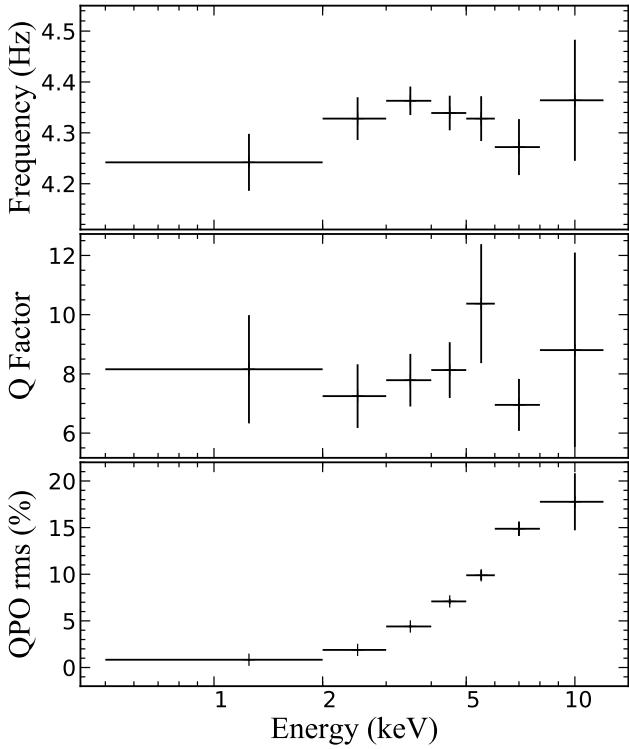| ObsID	Total Count Rate (counts s^{-1})	Num_Det_On	QPO Fundamental			Second Harmonic		
			ν_0 (Hz)	Q	rms (%)	ν_0 (Hz)	Q	rms (%)
1200530110	24157	26	4.37 ± 0.03	7.93 ± 0.51	0.98 ± 0.03	8.54 ± 0.32	5.15 ± 4.03	0.40 ± 0.07
1200530113	20177	23	4.48 ± 0.04	8.13 ± 1.44	1.59 ± 0.06	8.89 ± 0.18	5.89 ± 2.53	0.89 ± 0.02
1200530117	20608	26	4.30 ± 0.02	8.14 ± 0.86	1.48 ± 0.04	8.57 ± 0.23	8.07 ± 5.60	0.58 ± 0.08
1200530125	27283	41	4.06 ± 0.01	6.40 ± 0.36	1.37 ± 0.02	8.57 ± 0.25	3.90 ± 1.65	0.52 ± 0.07

Figure 5. Energy dependence of the frequency, *Q* factor, and fractional rms of the type-B QPO observed in Obs #3: 1200530117.

(2020): the QPO fractional rms increases from ∼1% at below 2 keV to ∼20% at around 10 keV.

The average PDS of epoch NQ are dominated by weak (≲1% in the 0.1–20 Hz frequency range) broadband noise without showing any narrow peak, similar to that usually observed in the SS of BHBs. To test the possibility of the presence of a QPO, we fitted the average PDS of epoch NQ using a Lorenzian function with the characteristic frequency and *Q* factor fixed at the values of the type-B QPO detected in that observation. We measured a 3-σ upper limit on the fractional rms of 0.31%, 0.47%, 0.55% and 0.52% for the four observations, respectively.

3.1.3 *Spectral difference*

To check the possible spectral changes during the transition, we extracted spectra from the period with and without the type-B QPO separately. Hereafter we refer to them as the BQ spectrum and the NQ spectrum, respectively. In order to take advantage of the large amount of photons detected by *NICER*, we first extracted spectra accumulated from the orbits with and without the QPO, for each observation. The BQ (red) and NQ (black) spectra and corresponding spectral ratio (BQ/NQ) are shown in Fig. 6. This figure shows that even if the shape of the BQ (or NQ) spectrum is different between observations (also see the spectral fits in section 3.2), the shape of the spectral ratio is remarkably similar in all cases. The main difference appears at energy bands above 2 keV (but note that the ratio is not constant below 2 keV), where the spectral ratio increases gradually towards higher energies. This indicates the presence of a stronger hard component when the type-B QPO was detected. The value of the spectral ratio is much larger in Obs #2 and #3 (above 1.5 at 10 keV) than that in Obs #1 and #4 (around 1.15 at 10

keV). Below 2 keV, the spectral difference is subtle. Upon inspection, we found a slightly increasing trend towards lower energies, which is likely associated with variations in the disk component. The overall spectral ratio below 2 keV is smaller than unity, suggesting that the disk component is weaker during the appearance of the type-B QPO. In Obs. #1, the type-B QPO disappeared in the first three orbits, and reappeared in orbit 4, and then disappeared again in orbit 5. We compared the spectra of orbits 3 and 5. The spectra before the appearance of the type-B QPO and after its disappearance are the same within errors.

We note that the hardness ratio during the period with/without the QPO changes significantly in some observations (see Fig. 2), indicating spectral changes. To reduce the effect of these spectral changes, we also compared the BQ and NQ spectra by extracting the energy spectra from a single orbit (or two if its net exposure time is less than 150 s) before and after the transition. The unfolded spectra and corresponding spectral ratio are shown in Fig. 7. The shape of the spectral ratio is consistent with that obtained from the average spectra.

3.2 Spectral modelling

3.2.1 *Fit with standard two-component continuum models*

In order to further study the spectral difference, we performed spectral modelling for the BQ and NQ spectra taking from one or two single orbits before and after the transition shown in Fig. 7. For each observation, we fitted the BQ and NQ spectra jointly using two different models:

Model 1: TBNEW*(SIMPL*DISKBB+GAUSSIAN), and **Model 2:** TBNEW*(DISKBB+NTHCOMP+GAUSSIAN).

In both models, the absorption along the line of sight was modelled using TBNEW[2], which is a high resolution version of the X-ray absorption model TBABS. All abundances were fixed at the solar value given by Wilms et al. (2000)[3]. The DISKBB component is a multi-temperature blackbody model accounting for emission from a geometrically thin, optically thick accretion disk (Shakura & Sunyaev 1973). Both SIMPL (Steiner et al. 2009) and NTHCOMP (Zdziarski et al. 1996) describe the power-law like continuum produced by thermal Comptonisation of soft disk photons in a hot gas of electrons. SIMPL is developed as a convolution model with two free parameters, i.e., the photon index, Γ, and the scattered fraction, f_{sc}; whereas NTHCOMP is used as an additive model. In model 2, we assumed that all the seed photons for the Comptonised component are produced by the disk and linked the seed photon temperature of the NTHCOMP component, kT_{bb}, to the inner disk temperature of the DISKBB component, kT_{in}. Since the high-energy cutoff of the Comptonised component is outside the *NICER* energy range, we fixed the electron temperature at 1000 keV. Therefore, the free parameters of the NTHCOMP component are the photon index (Γ) and the normalisation ($N_{nthcomp}$). In both models, a GAUSSIAN line was added to account for the weak Fe Kα emission line seen in the spectra. In some cases, the line energy or width was fixed since the parameters could not be constrained very well. We allowed all the parameters

---

[2] https://pulsar.sternwarte.uni-erlangen.de/wilms/research/tbabs/

[3] Note that in Paper-I, the abundances we used are from Anders & Grevesse (1989). As a result, the N_H is lower than that measured in this work.

Obs #1: 1200530110

Obs #2: 1200530113

Obs #3: 1200530117
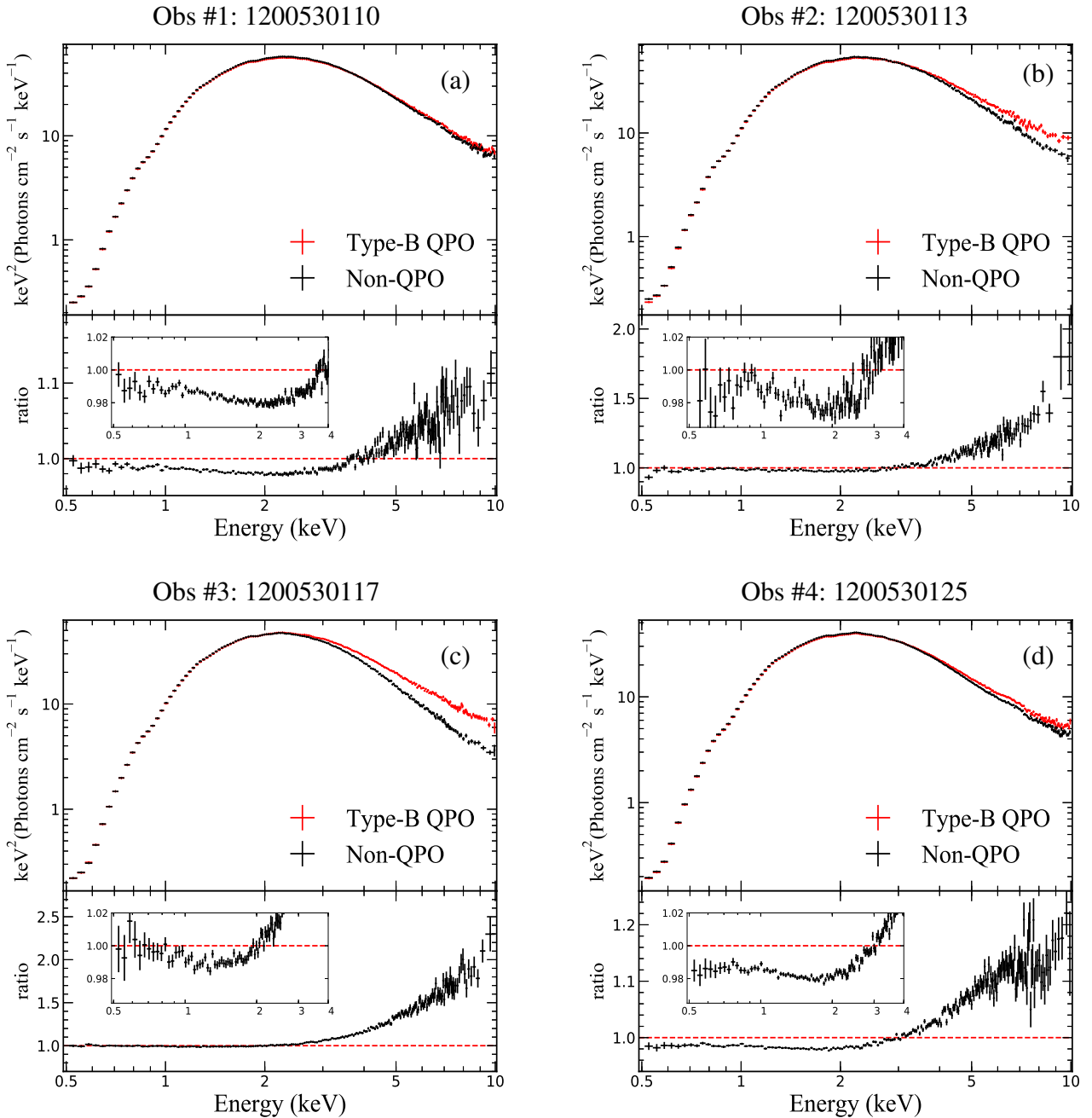
Obs #4: 1200530125

Figure 6. Unfolded spectra of the period with (red) and without (black) a type-B QPO, and corresponding spectral ratio defined as the ratio between the spectrum with the type-B QPO and that without the QPO (type-B/non-QPO). The spectra were extracted from all the orbits with and without the type-B QPO, respectively, and deconvolved against a power law with $\Gamma = 2$.

to vary between the two epochs except for the equivalent hydrogen column density, $N_{\rm H}$, which was kept linked. We calculated the 0.6–10 keV unabsorbed fluxes of different components using CFLUX from model 2. The best-fitting spectral parameters for models 1 and 2 are listed in Table 3. Both models give acceptable spectral fits with $\chi^2/{\rm dof} < 1.1$. In Fig. A1 and A2, we show an example of the distributions of the main best-fitting spectral parameters for models 1 and 2, respectively. For completeness, we also fitted the spectra taken from all the orbits with/without the QPO (shown in Fig. 6) with models 1 and 2. We show the best-fitting results in Table A1.

The main conclusions of this paper are the same if we either fit the average or the single-orbit spectra.

From epoch NQ to BQ, the inner disk temperature decreased marginally in all cases for both models 1 and 2. The behaviour of the DISKBB normalisation, $N_{\rm diskbb}$, which is related to inner disk radius ($N_{\rm diskbb} \propto R_{\rm in}^2$), depends on the model we used. When using model 2, $N_{\rm diskbb}$ decreased from epoch NQ to BQ in all cases, suggesting that the inner disk front is closer to the central BH during the appearance of the type-B QPO. However, when using model 1, $N_{\rm diskbb}$ increased from epoch NQ to BQ in all cases. SIMPL outputs the sum of the unscattered seed photon spectrum

Obs #1: 1200530110

(a)

Orbit 4 (BQ)
Orbit 3 (NQ)

Obs #2: 1200530113

(b)

Orbit 2&3 (BQ)
Orbit 4 (NQ)

Obs #3: 1200530117

(c)

Orbit 5 (BQ)
Orbit 4 (NQ)

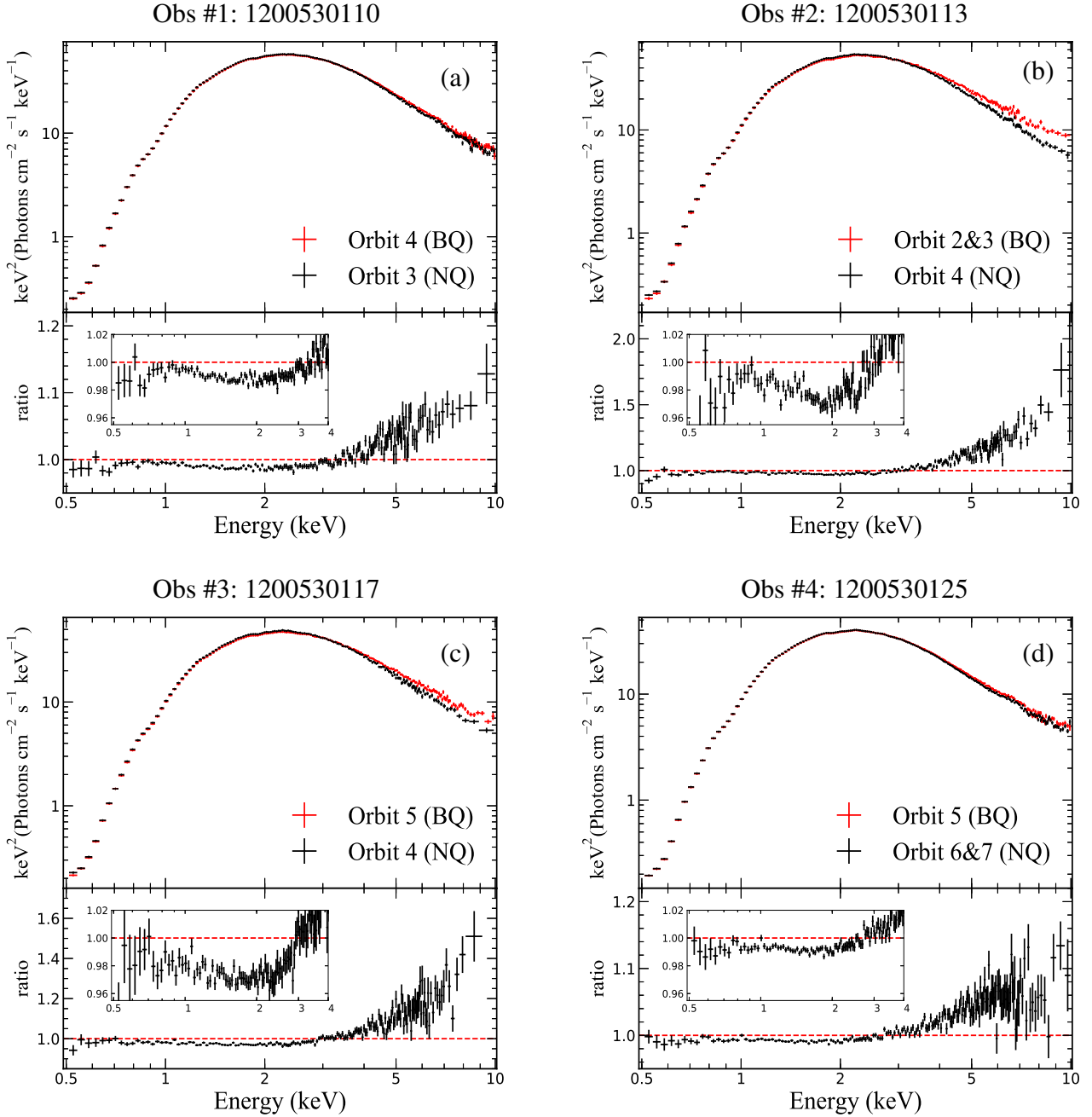## Obs #4: 1200530125

(d)

Orbit 5 (BQ)
Orbit 6&7 (NQ)

Figure 7. Same as Fig. 6. However, the spectra of the period with and without the type-B QPO were extracted from one or two single orbits before and after the transition.

and the scattered power-law component. The input seed spectrum of photons (DISKBB in our case) is multiplied by $(1 - f_{sc})$ before adding it back to the scattered power-law component which contains f_{sc} times the number of photons as in the DISKBB. Thus the fitted N_{diskbb} is not the one that is directly measured, and the model effectively assumes that the disk is screened by the Comptonised region, with only $(1 - f_{sc})$ leaking through. The increase in N_{diskbb} from epoch NQ to BQ might be artificially induced to account for the drop in direct photons due to the rise in f_{sc}. In an attempt to make the disk normalisation independent of this underlying assumption made by SIMPL, we used an alternative set up by fitting the data with the model TBNEW*(SIMPL*DISKBB+CONSTANT*DISKBB+GAUSSIAN). The

disk normalisation and temperature were linked and the scattered fraction of the SIMPL model was fixed at unity. In this way, the disk normalisation and the SIMPL component are not tied, and the CONSTANT will allow the DISKBB to vary freely. The best-fitting spectral parameters of our modelling are reported in Table A2. We found similar results as those reported for model 1, except that N_{diskbb} for both epoch BQ and NQ is much lower than what we found using model 1.

Back to our results of using models 1 and 2, we found that the photon index does not change significantly between epoch BQ and NQ. The best-fitting Γ obtained is consistent between the two epochs within errors, except in the case of Obs #1, where the Γ is slightly
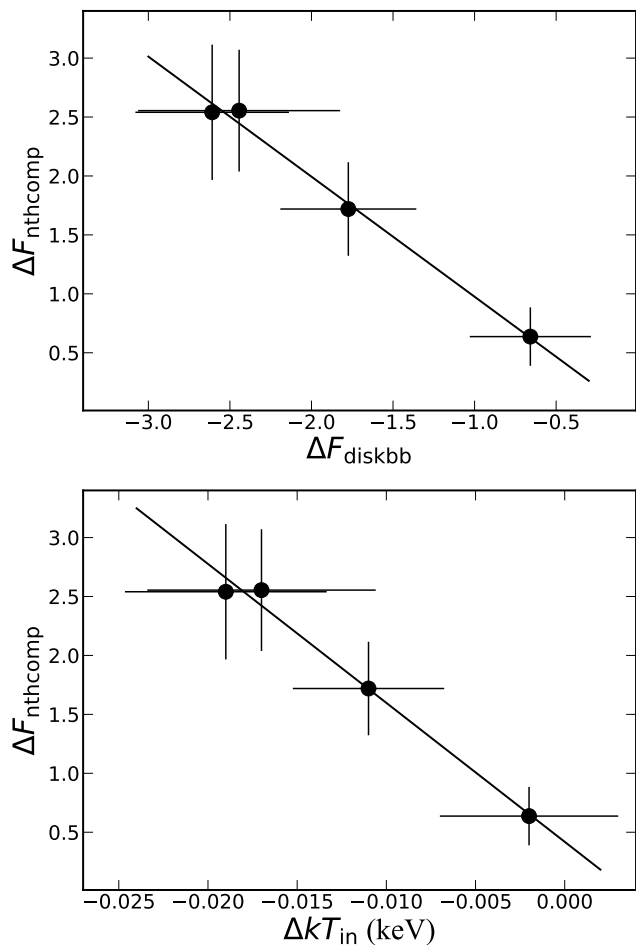
Figure 8. The change of the Comptonised component flux ($\Delta F_{\mathrm{nthcomp}}$) as a function of the change of the disk component flux (upper, $\Delta F_{\mathrm{diskbb}}$) and the change of the inner disk temperature (lower, ΔkT_{in}) from non-QPO to type-B QPO. The spectra of the period with and without the type-B QPO were extracted from one or two single orbits before and after the transition. The fluxes of different components and the inner disk temperature were measured from model 2. The fluxes are in units of 10^{-8} erg cm^{-2} s^{-1}. The solid line represents the best-fittinting straight line ($y = -1.02x - 0.04$ for the upper panel and $y = -117.89x + 0.42$ for the lower panel) to the data.

larger for epoch BQ. However, the scattered fraction changed significantly by 26%, 30%, 36%, 15% for the four cases, respectively. This result suggests that the increased hardening is related to an increase in normalisation of the hard component (e.g., due to an increase in scattered fraction of the Comptonised component), rather than a change in slope. In addition, we note that the Γ we measured is higher ($\Gamma \approx 3 - 3.5$) than the expected value ($\Gamma \approx 2.2 - 3$) typically observed during the SIMS in other BHBs (e.g., Remillard & Mc-Clintock 2006). This is possibly because the photon index cannot be well constrained due to the narrow bandpass of *NICER*.

The Fe Kα emission line was weak during the period we analysed here. The contribution of the line to the total flux is $\lesssim 0.2\%$ in all cases. The parameters of the GAUSSIAN component do not show substantial variations from epoch NQ to BQ. Linking the GAUSSIAN component between the two epochs does not worsen the fits. Fitting the iron line with more complicated models is beyond the scope of this paper, and does not affect the main conclusions of this work.
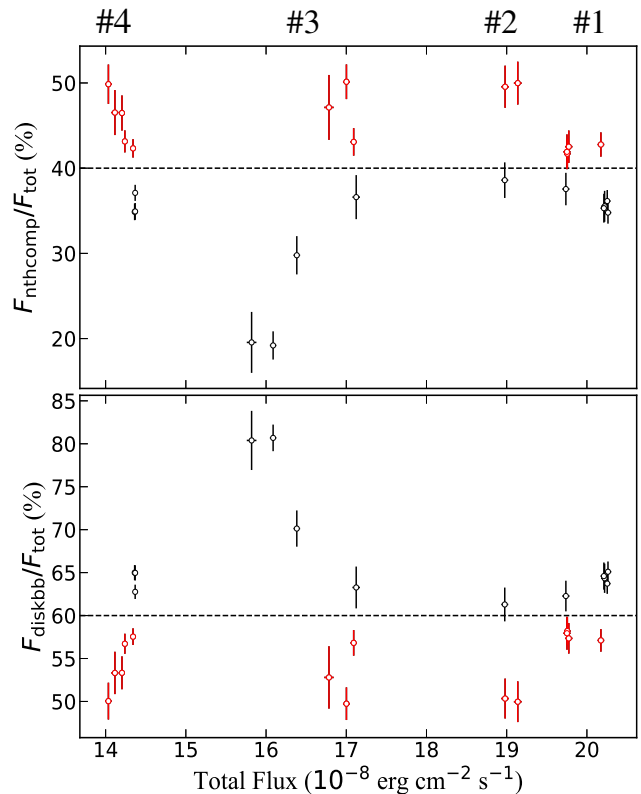
A key difference we found when comparing the BQ and NQ

Figure 9. Flux fraction of the Comptonised component ($F_{\mathrm{nthcomp}}/F_{\mathrm{total}}$, upper) and the disk component ($F_{\mathrm{diskbb}}/F_{\mathrm{total}}$, lower) as a function of the total flux for each orbit of the four observations in which a fast appearance/disappearance of a type-B QPO was observed. Each data point represents the result of one or two single orbits. The red (black) points represent the orbits with (without) a type-B QPO. Note that some of the data points are overlapped.

spectra is in the fluxes of the disk and Comptonised components. From epoch NQ to BQ, the disk component flux decreased, while the Comptonised component flux increased in all cases. This can be inferred from the rise in scattered fraction (f_{sc}) when using model 1, meaning that a larger fraction of seed photons are scattered into the Comptonised component during the appearance of the type-B QPO. In Fig. 8, we plot the change of the Comptonised component flux ($\Delta F_{\mathrm{nthcomp}}$), as a function of the change of the disk component flux ($\Delta F_{\mathrm{diskbb}}$) and the change of the inner disk temperature (ΔkT_{in}) from epoch NQ to BQ. We found that $\Delta F_{\mathrm{nthcomp}}$ is anti-correlated with $\Delta F_{\mathrm{diskbb}}$ and ΔkT_{in}.

To find out which set of spectral parameters are responsible for the spectral difference, we fitted the BQ and NQ spectra of each observation simultaneously with all the parameters tied at first. Then, we allowed the parameters of the Comptonised, disk, and GAUSSIAN components free one by one, and studied the change in χ^2/dof. The resulting χ^2/dof is shown in Table 4. As expected, if all the parameters were tied, then we obtained very poor spectral fits with χ^2/dof $\gtrsim 1.9$ (sometimes χ^2/dof > 3). Allowing the parameters of the Comptonised component to vary between epochs BQ and NQ brings significant improvement to the fits. In general, this produces an improvement of $\Delta\chi^2 \gtrsim 300$ through the addition of two free parameters. In all cases, freeing Γ first results in a better fit than freeing f_{sc} (model 1) or N_{nthcomp} (model 2) first. However, only untying the parameters of the Comptonised component is not
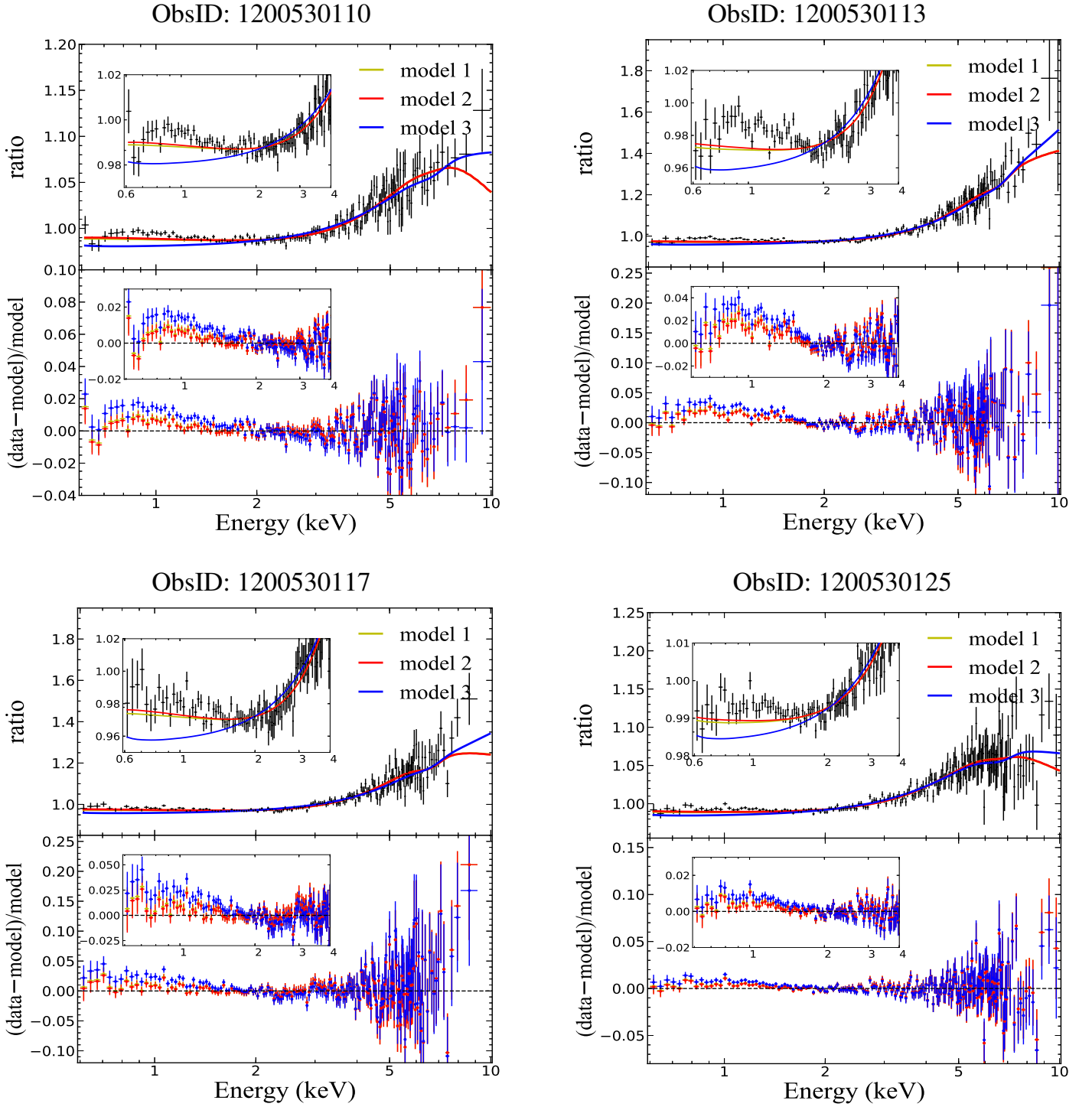
Figure 10. *Upper panels:* data-points represent the ratio between the spectra with and without the type-B QPO. In a similar way, yellow, red and blue lines correspond to the ratio of the best-fitting models for the spectra with and without the QPO for our models 1, 2 and 3, respectively. Insets show a zoom to the low-energy region. *Lower panels:* the ratio (DATA−MODEL)/MODEL for models 1, 2 and 3 (yellow, red and blue, respectively), where DATA and MODEL are, respectively, the ratios of the spectra and models plotted in the upper panels. The error bars in the lower panels are underestimated, as we do not consider the errors in the model (i.e. we assume the models are perfect). Insets show a zoom to the low-energy region. Note that in this figure models 1 and 2 are overlapped.

enough to model the overall spectral difference. Variations in the DISKBB component are also required. In model 1, allowing kT_{in} and N_{diskbb} to be free improves the fits by $\Delta\chi^2 \gtrsim 90$; while in model 2, this improves the fits by $\Delta\chi^2 \gtrsim 30$. The two parameters of DISKBB were highly degenerate. It is hard to distinguish the parameter that leads to the changes. When using model 1, freeing kT_{in} first results in a slightly lower reduced χ^2 than freeing N_{diskbb} first; in contrast, when using model 2, freeing N_{diskbb} first is better than freeing kT_{in} first. Allowing the parameters of the GAUSSIAN component to be free did not improve the fits.

From our spectral analysis above, we found that the appearance of the type-B QPO is related to a change in the relative contribution of the disk and Comptonised emission. In Fig. 9, we show the fraction of the Comptonised component flux to the total flux ($F_{nthcomp}/F_{total}$, upper) and the fraction of the disk component flux to the total flux (F_{diskbb}/F_{total}, lower) against the total flux. In this plot, each data point represents the result from one or two single orbits. The red/black points mark the orbits with/without the type-B QPO. We found a very clear threshold in $F_{nthcomp}/F_{total}$ or F_{diskbb}/F_{total} which is related to the appearance of the type-B QPO. When $F_{nthcomp}/F_{total} \gtrsim 40\%$ (or $F_{diskbb}/F_{total} \lesssim 60\%$), the type-B QPO was observed. However, when $F_{nthcomp}/F_{total} \lesssim 40\%$ (or $F_{diskbb}/F_{total} \gtrsim 60\%$), the type-B QPO disappeared.

3.2.2 Fit with a two-component Comptonisation model

García et al. (2021) found that the energy-dependent fractional rms and phase lags of the type-B QPO in MAXI J1348−630 can be well modelled with a two-component Comptonisation model. Given that Figs. 6 and 7 show that the emission above 2 keV is stronger when the type-B QPO appears, then it is natural to consider that either the number of spectral components does not change (but only their parameters), or that the appearance of the type-B QPO is related to the appearance of an additional spectral component. The first scenario was studied in the previous section. In this section, we further investigate the possibility that the type-B QPO originates from an additional Comptonised component.

For each observation, we fitted the BQ and NQ spectra simultaneously with a two-component Comptonisation model:

Model 3: TBNEW*(CONSTANT*(DISKBB+NTHCOMP$_1$+ GAUSSIAN)+NTHCOMP$_2$).

In this model, we assume that the DISKBB, NTHCOMP$_1$ and GAUSSIAN components are present in the spectra of both epochs, and these components have the same spectral shape with all parameters linked. The only difference is in their fluxes which is accounted for by using a CONSTANT. The CONSTANT was fixed at unity for epoch NQ and was allowed to vary for epoch BQ. The NTHCOMP$_2$ component is assumed to be associated with the QPO and only contributes to the spectrum of epoch BQ. The normalisation of this component, $N_{nthcomp2}$, for epoch NQ was fixed at zero. In both NTHCOMP$_1$ and NTHCOMP$_2$, the seed photon temperature, kT_{bb}, was linked to the inner disk temperature of the DISKBB component, kT_{in}. The electron temperature was fixed at 1000 keV. The best-fitting spectral parameters for model 3 are presented in Table 5. Model 3 provides an slightly worse fit than model 2 for Obs. #1, #2 and #3, and an approximately equivalent fit for Obs. #4.

In model 3, compared with the same setting without the NTHCOMP$_2$ component, adding this component for epoch BQ reduces the χ^2 significantly by $\Delta\chi^2 > 400$ for 2 degrees of freedom (dof) less, which yields an F-test probability of $\ll 10^{-10}$. At the

same time, the value of $N_{nthcomp2}$ measured is more than 4.6σ different than zero[4]. From all these we conclude that this component is significantly required for the BQ spectrum. The value of $N_{nthcomp2}$ for epoch NQ was fixed at zero at first. If we then let it be free, the best-fitting value of this parameter is consistent with zero, which indicates that this component is not needed in the NQ spectrum.

The disk temperature and normalisation measured from model 3 is similar to that of model 2 for epoch NQ. In Obs #2 and #3, where the spectral ratio above 2 keV is much larger than that of the other two cases, the photon index of NTHCOMP$_2$ is significantly smaller than that of NTHCOMP$_1$, suggesting that the Comptonised component associated with the QPO is harder. While in Obs. #1 and #4, where the spectral ratio above 2 keV is smaller, the photon index is consistent between the two Comptonised components within errors.

In Fig. 10 we show the ratio between the best-fitting models of the BQ and NQ spectra for each of the models we used. It can be seen that the two-component Comptonisation model (model 3) fits the spectral ratio better at high energy bands. However, none of the models we used can fully account for the small difference of the spectra below 2 keV, even if we allowed the disk temperature and normalisation to vary between epoch BQ and NQ. The small difference appears systematically in all four observations, and it is likely real. We note that *NICER* spectra shows calibration-related instrumental residuals below 2 keV (see, e.g., Ludlam et al. 2018). However, the spectral ratios we have shown in the lower panel of Fig. 6 and 7 are not affected by the instrumental residuals.

4 DISCUSSION

Fast transitions in X-ray variability are rare events. In the past two decades there have only been reports for three sources, with a relatively large number of detections in XTE J1859+226 (Casella et al. 2004; Sriram et al. 2013), H1743−322 (Sriram et al. 2021) and GX 339−4 (Nespoli et al. 2003; Motta et al. 2011). While the small number of detections in other BHBs is probably intrinsic to the systems, it is also partly due to the limitation on the observation coverage. The multiple detection of the fast transition between non-QPO and type-B QPO in MAXI J1348−630 has allowed us to perform the first systematic spectral-timing analysis of such a transition in a source, and the first study with spectral information in the 0.5–2 keV range. Our main results can be summarized as:

• the overall spectral hardness is slightly higher (harder) when the type-B QPO was detected;

• the main spectral difference between the period with and without the type-B QPO was seen at energies above 2 keV, and it is very small below 2 keV;

• during the transition from non-QPO to type-B QPO, both the disk and Comptonised fluxes changed significantly and they varied in an anti-correlated way. However, the total flux of the source in the 0.5–12 keV band remained relatively stable during the transition.

4.1 Spectral difference above and below 2 keV

Stevens & Uttley (2016) studied the type-B QPO in GX 339−4 using phase-resolved spectroscopy. They found that the disk and power-law emission varied with ~1.4 per cent and ~25 per cent

---

[4] the best-fitting $N_{nthcomp2}$ divided by its 1-σ error.

rms, respectively, in the QPO cycle. The variability of the disk flux is very small, similar to the value of the QPO fractional rms we measured at energies below 2 keV (about 0.9 per cent, see Fig. 5). Based on a systematic study of the type-B QPO in several BHBs, Gao et al. (2017) confirmed a positive correlation between the type-B QPO frequency and the Comptonised component flux, which was first reported in GX 339−4 by Motta et al. (2011).

By comparing the spectra of the period with and without the type-B QPO, we found that the main spectral difference comes from energies above 2 keV where the emission is dominated by the Comptonised component. Our spectral fits confirmed that the variations of the Comptonised component parameters are responsible for the main spectral difference. These results are consistent with the findings of Stevens & Uttley (2016) and Gao et al. (2017) that the Comptonised component dominates the type-B QPO emission.

At low energies (below 2 keV), the spectral difference is small. The spectral ratio below 2 keV is not constant within errors, indicating a change in the flux as well as the spectral shape. From our joint fits with models 1 and 2, we also found that both the disk and Comptonised components are required to vary during the transition, although the variations of the DISKBB parameters are very small compared to the changes of the Comptonised component. In the lower panels of Fig. 10 we show that while the models we used here fit the data well, they still fail to correctly fit an excess at energies below 2 keV. This excess appears systematically in all four observations, and they are only ∼2–4 per cent deviations from the models we used. We tried to model that excess with another BLACKBODY component, however the model did not converge and the fits became unstable. The reason why we are unable to constrain this small excess below 2 keV is probably related to the lack of broad-band coverage (which prevent us to fit the full reflection models), and the fact that ∼2 per cent excess is at the limit of the current NICER calibration, and therefore it is unclear how well this excess can be constrained. However, we note that the small excess should not affect the best-fitting spectral parameters and the threshold in the relative contribution of the disk and Comptonised emission significantly.

4.2 Flux variation during the transition and the transient nature of the type-B QPO

Nespoli et al. (2003) reported a fast appearance of a 6-Hz type-B QPO in GX 339−4 with an increase in source flux. The PDS of the period without the type-B QPO showed a broad peak at around 7 Hz, which is likely to be a type-A QPO. During the transition from the potential type-A to type-B QPO, the disk flux decreased by 9 per cent, while the power-law flux increased by 30 per cent. Fast transitions between type-A and type-B QPO were also detected in XTE J1859+226 (Casella et al. 2004; Sriram et al. 2013) and XTE J1817−330 (Sriram et al. 2012) with *RXTE*. We note that such transitions are often associated with a sudden change in source flux. In the two cases of XTE J1859+226, both the disk and power-law fluxes decreased in one case (ObsID: 40124-01-13-00) and increased in the other case (ObsID: 40124-01-14-00) from type-A to type-B QPO. In the case of XTE J1817−330, the period with the type-B QPO has a higher flux than that with the type-A QPO, and the flux change is due to the power-law component (the disk flux does not change). Type-C to/from type-B QPO transitions have been observed in a few sources (e.g., Casella et al. 2004; Motta et al. 2011; Homan et al. 2020; Sriram et al. 2021), which correspond to the state transition between the HIMS and SIMS. These transitions also involve a flux change, and the type-B QPOs are always present

at a higher flux level. Xu et al. (2019) detected a sudden turn-on of a transient type-C QPO in Swift J1658.2−4242 with a rapid flux drop. During the transition, both the disk and power-law fluxes decrease. Similar transient type-C QPOs were also found in three *RXTE* observations of H1743−322 (Sriram et al. 2021). However, no consistent flux change was seen during these transitions. The turn-on of the type-C QPO was accompanied by a flux rise in ObsID 80146-01-07-00, and a flux drop in ObsID 80146-01-13-00 and 80146-01-50-00.

Sriram et al. (2013) reported a non-QPO to type-B QPO transition observed in XTE J1859+226 (ObsID: 40122-01-01-00). All the parameters except the photon index are required to vary when fitting the spectra of the period with and without the QPO with a disk and a power-law component. More recently, Sriram et al. (2021) found a transient 4.5-Hz type-B QPO in three *RXTE* observations of H1743−322. In all those cases, the disk flux decreased while the power-law flux increased during the transition from non-QPO to type-B QPO, similar to what we found in MAXI J1348−630.

As shown in Fig. 2, the 0.5–12 keV count rate (total flux) of MAXI J1348−630 remained more or less constant from non-QPO to type-B QPO. In addition, we found that both the disk and Comptonised component fluxes change significantly during the transition, and the change of the disk component flux (or kT_{in}) is anti-correlated with that of the Comptonised component flux. It is worth mentioning that the flux change can be inferred from the spectral ratio shown in Fig. 6 and 7, which is model independent. Our results reveal the transient nature of the type-B QPO: the type-B QPO is associated with a redistribution of accretion power between the disk and Comptonised emission. Compared with the period without the QPO, a larger fraction of accretion power is dissipated into the Comptonised region than in the disk when the type-B QPO appears.

From Fig. 2, we found that the orbits with the type-B QPO always correspond to a slightly higher hardness ratio within each observation. However, the hardness value corresponding to the transition is different between observations. From Fig. 9, we can see that it is the relative contribution of the disk and Comptonised emission that determines the appearance of the QPO, rather than the value of the hardness ratio. A very sharp threshold in the flux fraction of the disk/Comptonised component was observed. The type-B QPO was only detected when the contribution of the Comptonised emission to the total flux is above ∼40 per cent in the 0.6–10 keV band. Below this threshold, the type-B QPO switched off. At present, we do not know if the critical value is the same in all BHBs, or whether source properties determine this critical value.

4.3 Origin of the type-B QPO

Although no comprehensive model has been proposed for the type-B QPOs, there is growing evidence suggesting that they may originate in a jet-like structure. The most striking observational evidence is the fact that the launch of discrete jet ejection (or the resulting radio flare) occurs close in time to the appearance of the type-B QPO, which has been found in a few BHBs (Soleri et al. 2008; Fender et al. 2009; Russell et al. 2019a; Homan et al. 2020; Russell et al. 2020). However, the precise association between the ejection event and the type-B QPO is not clear, as the type-B QPO sometimes appears before and sometimes after the inferred jet ejection. The main obstacle of these studies is the gaps in the X-ray/radio coverage. The strongest evidence to date was provided by Homan et al. (2020) who found that the start time of the radio flare is ∼2–2.5 hr after the appearance of the type-B QPO in MAXI J1820+070. In addition, Homan et al. (2020) found that the appearance of the type-B QPO

coincides with the start of a brief X-ray flare in the *NICER* 7–12 keV band. The X-ray flare can possibly be due to the contribution to the X-ray flux from the jet. In MAXI J1348−630, a strong radio flare was observed on MJD 58523 (Carotenuto et al. 2021), which is close to the time when the type-B QPOs started to be detected (MJD 58522.6, Paper-I). The radio flare is likely to be associated with a discrete jet ejection with its best inferred ejection date $t_{\rm ej}$ = MJD 58518.9 ± 2.4 (Carotenuto et al. 2021). This suggests a strong connection between the radio flare (or jet ejection) and the type-B QPOs we observed.

The jet-based origin of the type-B QPO was also supported by the fact that the type-B QPOs are stronger in low-inclination (face-on) sources (Motta et al. 2015). To explain the small amplitude of the disk varations and its phase relation to the power-law emission, Stevens & Uttley (2016) proposed that the Comptonised region producing the type-B QPO has a relatively large scale-height, such as the base of the jet. Stevens & Uttley (2016) also found that the power-law photon index varies between ~2.3 and ~2.6 within the QPO cycle, which can be quantitatively explained by a precessing jet model (Kylafis et al. 2020). Such a precessing jet has already been seen in 3D general relativistic magnetohydrodynamic simulations (Liska et al. 2018).

As shown in Fig. 6 and 7, a stronger Comptonised component was seen when the type-B QPO was detected. Although we cannot rule out the one Comptonised component models, our successful spectral fit with a two-component Comptonised model suggests that the increased Comptonised emission may come from an additional component that is only present when the type-B QPO appears. Given its direct association with the type-B QPO, this component may be related to the jet.

The energy-dependent fractional rms and phase lags of the type-B QPO in MAXI J1348−630 have been explained by a two-component Comptonisation model (García et al. 2021). In this model, each Comptonisation component dominates the variability observed in the QPO in different energy ranges. Considering the dilution caused by the disk-blackbody soft-thermal emission, the model indicates that a *large* component (~550 R_g) dominates the low-amplitude variability ($\lesssim$ 5%) below 4–5 keV, whereas above 4–5 keV, where the amplitude variability is larger (~5–15%), a *small* component (~20 R_g) prevails. Significant illumination of the accretion disk by an extended Comptonised region is also expected in jet models (Reig & Kylafis 2021).

If such a large Comptonised region is present, a narrow Fe K line would be expected in the spectrum if this component illuminates the outer parts of the disk, together with a broad line produced by the small component illuminating the inner parts of the disk. Such an effect was found by García et al. (2019) during the 2017 failed-transition outburst of GX 339–4. In that work, the authors showed that the spectral fits are significantly improved by invoking a dual-lampost model, where the lampost component that is farthest away has a height of 500–700 R_g. In our spectra we clearly see a broad Fe K line. To check the possibility of the presence of a narrow line, we combined all the BQ segments (with the type-B QPO active) and added a narrow Gaussian with width fixed at 0.01 and 0.1 keV to model 1. We obtained 3-σ upper limits of 2.5 and 4.7 eV, respectively, to the presence of such a narrow Fe line. We then performed simulations using a combination of `relxill` and `xillver` models (García et al. 2014), corresponding to a corona at 20 and 500 R_g above the disk, respectively, and found consistent upper limits to such a narrow line. The potential narrow line connected to the appearance of the type-B QPO would strongly support such an extended Comptonisation region. On the contrary, more stringent constrains on the presence of such a narrow Fe line could strongly constrain those models.

5   CONCLUSION

In Summary, in this work we have presented the first systematic spectral-timing analysis of a fast appearance/disappearance of a type-B QPO in MAXI J1348−630 using *NICER* data. We measured the spectral difference between the periods with and without the QPO, and confirmed that the QPO emission is dominated by the hard component. Compared with the period without the QPO, the Comptonised emission increased and the disk emission decreased when the type-B QPO was detected. This suggests that the transient nature of the type-B QPO is related to a redistribution of accretion power between the disk and Comptonised emission. It is important to mention again that our results focus on the energy bands below 10 keV. Future studies using broad-band X-ray data (e.g. 0.3-100 keV) will be able to better constrain the different spectral components (specially the hard and the reflection components), and give deeper insights into the origin of the QPOs. This would be possible if similar transitions to those presented in this paper are observed simultaneously with *NICER* and NuSTAR (Harrison et al. 2013), or *NICER* and *Insight*/HXMT (Zhang et al. 2020a).

Table 3. Best-fitting spectral parameters for models 1 and 2. The spectra of the period with and without the type-B QPO were extracted from one or two single orbits before and after the transition.

Component	Parameters	1200530110		1200530113		1200530117		1200530125	
		type-B QPO orbit 4	non-QPO orbit 3	type-B QPO orbit 2&3	non-QPO orbit 4	type-B QPO orbit 5	non-QPO orbit 4	type-B QPO orbit 5	non-QPO orbit 6&7
					Model 1: TBNEW*(SIMPL*DISKBB+GAUSSIAN)				
TBNEW	N_H ($\times 10^{22}$ cm^{-2})	0.89 ± 0.01		0.89 ± 0.01		0.89 ± 0.01		0.89 ± 0.01	
DISKBB	kT_{in} (keV)	0.693 ± 0.004	0.708 ± 0.004	0.671 ± 0.006	0.694 ± 0.005	0.650 ± 0.005	0.677 ± 0.005	0.640 ± 0.004	0.645 ± 0.003
	Norm	43441 ± 870	41048 ± 773	44783 ± 1447	41307 ± 980	46000 ± 1279	41631 ± 1197	43152 ± 1080	42578 ± 755
SIMPL	Γ	3.48 ± 0.04	3.30 ± 0.05	3.37 ± 0.06	3.46 ± 0.07	3.46 ± 0.05	3.37 ± 0.10	3.35 ± 0.05	3.27 ± 0.04
	f_{SC}	0.27 ± 0.01	0.20 ± 0.01	0.33 ± 0.02	0.23 ± 0.02	0.33 ± 0.02	0.21 ± 0.02	0.26 ± 0.01	0.22 ± 0.01
GAUSSIAN	E_{line} (keV)	6.4^a	6.4^a	6.4^a	6.4^a	6.4^a	6.4^a	6.42 ± 0.13	6.48 ± 0.08
	σ (keV)	0.56 ± 0.10	0.62 ± 0.12	0.5^a	0.5^a	0.5^a	0.5^a	0.57 ± 0.13	0.49 ± 0.09
	Norm	0.024 ± 0.006	0.030 ± 0.007	0.017 ± 0.006	0.024 ± 0.005	0.016 ± 0.004	0.023 ± 0.006	0.021 ± 0.006	0.018 ± 0.004
	χ^2/dof	$422.2/447$		$462.9/445$		$461.9/436$		$457.6/445$	
					Model 2: TBNEW*(DISKBB+NTHCOMP+GAUSSIAN)				
TBNEW	N_H ($\times 10^{22}$ cm^{-2})	0.90 ± 0.01		0.89 ± 0.01		0.90 ± 0.01		0.89 ± 0.01	
DISKBB	kT_{in} (keV)	0.707 ± 0.003	0.718 ± 0.003	0.689 ± 0.005	0.706 ± 0.004	0.668 ± 0.004	0.687 ± 0.004	0.653 ± 0.004	0.655 ± 0.003
	Norm	27371 ± 266	29560 ± 224	24780 ± 541	28113 ± 372	25403 ± 450	29342 ± 469	27940 ± 221	29764 ± 217
NTHCOMP	Γ	3.35 ± 0.04	3.18 ± 0.05	3.25 ± 0.06	3.33 ± 0.07	3.34 ± 0.05	3.24 ± 0.09	3.23 ± 0.05	3.16 ± 0.04
	Norm	19.1 ± 0.9	14.5 ± 0.8	21.5 ± 1.4	15.7 ± 1.1	20.1 ± 1.1	13.6 ± 1.3	13.8 ± 0.8	12.1 ± 0.6
GAUSSIAN	E_{line} (keV)	6.4^a	6.4^a	6.4^a	6.4^a	6.4^a	6.4^a	6.34 ± 0.14	6.45 ± 0.09
	σ (keV)	0.58 ± 0.10	0.64 ± 0.12	0.5^a	0.5^a	0.5^a	0.5^a	0.66 ± 0.14	0.53 ± 0.11
	Norm	0.026 ± 0.006	0.032 ± 0.008	0.019 ± 0.006	0.025 ± 0.005	0.017 ± 0.004	0.024 ± 0.006	0.026 ± 0.007	0.020 ± 0.005
	χ^2/dof	$427.1/447$		$464.7/445$		$465.7/436$		$463.2/445$	
	$F_{diskbb}{}^b$	11.56	13.34	9.33	11.79	8.36	10.97	8.34	9.00
	$F_{nthcomp}{}^b$	8.59	6.87	9.68	7.13	8.65	6.10	5.97	5.33
	$F_{gaussian}{}^b$	0.03	0.03	0.02	0.03	0.02	0.02	0.03	0.02
	$F_{total}{}^b$	20.18	20.24	19.03	18.95	17.03	17.09	14.34	14.35

^{a} Fixed.
^{b} 0.6–10 keV unabsorbed flux in units of 10^{-8} erg cm^{-2} s^{-1}.

Table 4. Results of simultaneous spectral fits for models 1 and 2. The spectra of the period with and without the type-B QPO were extracted from one or two single orbits before and after the transition.

Parameters	1200530110 χ^2/dof	1200530113 χ^2/dof	1200530117 χ^2/dof	1200530125 χ^2/dof
Model 1: TBNEW*(SIMPL*DISKBB+GAUSSIAN)				
All tied	847/453	2244/450	1416/441	1026/452
Free Γ	599/452	998/449	989/440	549/451
Free $f_{\rm SC}$	548/451	699/448	663/439	547/450
Free $kT_{\rm in}$	428/450	469/447	470/438	459/449
Free $N_{\rm diskbb}$	423/449	464/446	463/437	458/448
All free	422/447	463/445	462/436	458/445
All tied	847/453	2244/450	1416/441	1026/452
Free $f_{\rm SC}$	680/452	1434/449	1218/440	609/451
Free Γ	548/451	699/448	663/439	547/450
Free $N_{\rm diskbb}$	434/450	475/447	478/438	463/449
Free $kT_{\rm in}$	423/449	464/446	463/437	458/448
All free	422/447	463/445	462/436	458/445
Model 2: TBNEW*(DISKBB+NTHCOMP+GAUSSIAN)				
All tied	852/453	2247/450	1420/441	1032/452
Free Γ	616/452	1094/449	1030/440	560/451
Free $N_{\rm nthcomp}$	472/451	493/448	497/439	522/450
Free $kT_{\rm in}$	472/450	493/447	497/438	520/449
Free $N_{\rm diskbb}$	428/449	465/446	467/437	464/448
All free	427/447	465/445	466/436	463/445
All tied	852/453	2247/450	1420/441	1032/452
Free $N_{\rm nthcomp}$	817/452	2103/449	1420/440	802/451
Free Γ	472/451	493/448	497/439	522/450
Free $N_{\rm diskbb}$	436/450	476/447	481/438	467/449
Free $kT_{\rm in}$	428/449	465/446	467/437	464/448
All free	427/447	465/445	466/436	463/445

Table 5. Best-fitting spectral parameters for model 3. The spectra of the period with and without the type-B QPO were extracted from one or two single orbits before and after the transition.

Component	Parameters	1200530110		1200530113		1200530117		1200530125	
		type-B QPO orbit 4	non-QPO orbit 3	type-B QPO orbit 2&3	non-QPO orbit 4	type-B QPO orbit 5	non-QPO orbit 4	type-B QPO orbit 5	non-QPO orbit 6&7
		Model 3: TBNEW*(CONSTANT*(DISKBB+NTHCOMP$_1$+GAUSSIAN)+NTHCOMP$_2$)							
TBNEW	N_H ($\times10^{22}$ cm^{-2})	0.90 ± 0.01		0.89 ± 0.01		0.90 ± 0.01		0.89 ± 0.01	
CONSTANT		0.94 ± 0.01	1^a	0.90 ± 0.01	1^a	0.89 ± 0.01	1^a	0.94 ± 0.01	1^a
DISKBB	kT_{in} (keV)	0.713 ± 0.002		0.699 ± 0.003		0.675 ± 0.003		0.654 ± 0.003	
	Norm	29380 ± 228		27604 ± 414		28528 ± 556		29733 ± 211	
NTHCOMP$_1$	Γ	3.27 ± 0.04		3.44 ± 0.06		3.45 ± 0.07		3.19 ± 0.03	
	Norm	16.0 ± 0.7		17.9 ± 1.1		17.2 ± 1.2		12.4 ± 0.5	
GAUSSIAN	E_{line} (keV)	6.4^a		6.4^a		6.4^a		6.41 ± 0.08	
	σ (keV)	0.61 ± 0.08		0.5^a		0.5^a		0.58 ± 0.10	
	Norm	0.030 ± 0.005		0.023 ± 0.004		0.021 ± 0.004		0.023 ± 0.005	
NTHCOMP$_2$	Γ	3.27 ± 0.19	-	2.52 ± 0.11	-	2.76 ± 0.14	-	3.36 ± 0.15	-
	Norm	2.3 ± 0.5	-	3.5 ± 0.4	-	3.3 ± 0.5	-	1.9 ± 0.3	-
	χ^2/dof	437.0/450		477.9/447		482.6/438		467.5/449	
	$F_{diskbb}{}^b$	12.08	12.83	9.95	11.11	8.82	9.86	8.41	8.93
	$F_{nthcomp_1}{}^b$	6.97	7.41	7.02	7.84	6.51	7.27	5.09	5.41
	$F_{gaussian}{}^b$	0.03	0.03	0.02	0.02	0.02	0.02	0.02	0.02
	$F_{nthcomp_2}{}^b$	1.06	-	1.98	-	1.65	-	0.81	-
	$F_{total}{}^b$	20.14	20.27	18.97	18.97	17.00	17.15	14.33	14.36

[a] Fixed.

[b] 0.6–10 keV unabsorbed flux in units of 10^{-8} erg cm^{-2} s^{-1}.

ACKNOWLEDGEMENTS

DATA AVAILABILITY

The data underlying this article are available in the HEASARC database.

REFERENCES

Anders E., Grevesse N., 1989, Geochimica Cosmochimica Acta, 53, 197
Belloni T., Hasinger G., 1990, A&A, 227, L33
Belloni T. M., Motta S. E., 2016, Transient Black Hole Binaries. SpringerVerlag, Berlin, p. 61
Belloni T. M., Zhang L., Kylafis N. D., Reig P., Altamirano D., 2020, MNRAS, 496, 4366
Bogensberger D., et al., 2020, A&A, 641, A101
Carotenuto F., et al., 2021, MNRAS,
Casella P., Belloni T., Homan J., Stella L., 2004, A&A, 426, 587
Chauhan J., et al., 2020, arXiv e-prints, p. arXiv:2009.14419
Denisenko D., et al., 2019, The Astronomer's Telegram, 12430, 1
Fender R. P., Homan J., Belloni T. M., 2009, MNRAS, 396, 1370
Gao H. Q., et al., 2017, MNRAS, 466, 564
García J., et al., 2014, ApJ, 782, 76
García J. A., et al., 2019, ApJ, 885, 48
García F., Méndez M., Karpouzas K., Belloni T., Zhang L., Altamirano D., 2021, MNRAS, 501, 3173
Gendreau K. C., et al., 2016, in Proc. SPIE. p. 99051H, doi:10.1117/12.2231304
Harrison F. A., et al., 2013, ApJ, 770, 103
Homan J., Belloni T., 2005, Ap&SS, 300, 107
Homan J., Wijnands R., van der Klis M., Belloni T., van Paradijs J., Klein-Wolt M., Fender R., Méndez M., 2001, ApJS, 132, 377
Homan J., et al., 2020, ApJ, 891, L29
Huang Y., et al., 2018, ApJ, 866, 122
Ingram A. R., Motta S. E., 2019, New Astron. Rev., 85, 101524
Ingram A., Done C., Fragile P. C., 2009, MNRAS, 397, L101
Jithesh V., Maqbool B., Misra R., T A. R., Mall G., James M., 2019, ApJ, 887, 101
Jithesh V., Misra R., Maqbool B., Mall G., 2021, arXiv e-prints, p. arXiv:2105.03066
Kennea J. A., Negoro H., 2019, The Astronomer's Telegram, 12434, 1
Kylafis N. D., Reig P., Papadakis I., 2020, A&A, 640, L16
Liska M., Hesp C., Tchekhovskoy A., Ingram A., van der Klis M., Markoff S., 2018, MNRAS, 474, L81
Ludlam R. M., et al., 2018, ApJ, 858, L5
Ma X., et al., 2021, Nature Astronomy, 5, 94
Miyamoto S., Kimura K., Kitamoto S., Dotani T., Ebisawa K., 1991, ApJ, 383, 784
Motta S. E., 2016, Astronomische Nachrichten, 337, 398
Motta S., Muñoz-Darias T., Casella P., Belloni T., Homan J., 2011, MNRAS, 418, 2292
Motta S. E., Casella P., Henze M., Muñoz-Darias T., Sanna A., Fender R., Belloni T., 2015, MNRAS, 447, 2059
Negoro H., et al., 2019, The Astronomer's Telegram, 12838, 1
Nespoli E., Belloni T., Homan J., Miller J. M., Lewin W. H. G., Méndez M., van der Klis M., 2003, A&A, 412, 235
Reig P., Kylafis N. D., 2021, A&A, 646, A112
Remillard R. A., McClintock J. E., 2006, ARA&A, 44, 49
Russell T. D., et al., 2019a, ApJ, 883, 198
Russell T., Anderson G., Miller-Jones J., Degenaar N., Eijnden J. v. d., Sivakoff G. R., Tetarenko A., 2019b, The Astronomer's Telegram, 12456, 1
Russell D. M., Casella P., Kalemci E., Vahdat Motlagh A., Saikia P., Pirbhoy S. F., Maitra D., 2020, MNRAS, 495, 182
Schnittman J. D., Homan J., Miller J. M., 2006, ApJ, 642, 420
Shakura N. I., Sunyaev R. A., 1973, A&A, 500, 33
Soleri P., Belloni T., Casella P., 2008, MNRAS, 383, 1089
Sriram K., Rao A. R., Choi C. S., 2012, A&A, 541, A6
Sriram K., Rao A. R., Choi C. S., 2013, ApJ, 775, 28
Sriram K., Rao A. R., Choi C. S., 2016, ApJ, 823, 67
Sriram K., Harikrishna S., Choi C. S., 2021, arXiv e-prints, p. arXiv:2103.02422
Steiner J. F., Narayan R., McClintock J. E., Ebisawa K., 2009, PASP, 121, 1279
Stevens A. L., Uttley P., 2016, MNRAS, 460, 2796
Takizawa M., et al., 1997, ApJ, 489, 272
Tominaga M., et al., 2020, ApJ, 899, L20
Wijnands R., Méndez M., Miller J. M., Homan J., 2001, MNRAS, 328, 451
Wilms J., Allen A., McCray R., 2000, ApJ, 542, 914
Xu Y., et al., 2019, ApJ, 879, 93
Yatabe F., et al., 2019, The Astronomer's Telegram, 12425, 1
Zdziarski A. A., Johnson W. N., Magdziarz P., 1996, MNRAS, 283, 193
Zhang S.-N., et al., 2020a, Science China Physics, Mechanics, and Astronomy, 63, 249502
Zhang L., et al., 2020b, MNRAS, 499, 851
Zhang L., et al., 2020c, The Astronomer's Telegram, 13465, 1
van den Eijnden J., Ingram A., Uttley P., Motta S. E., Belloni T. M., Gardenier D. W., 2017, MNRAS, 464, 2643

APPENDIX A: ADDITIONAL FIGURE AND TABLE

Figure A1. Distributions of the main best-fitting spectral parameters fitted with model 1: ᴛʙɴᴇᴡ*(sɪᴍᴘʟ*ᴅɪsᴋʙʙ+ɢᴀᴜssɪᴀɴ) for Obs. #1: 1200530110.
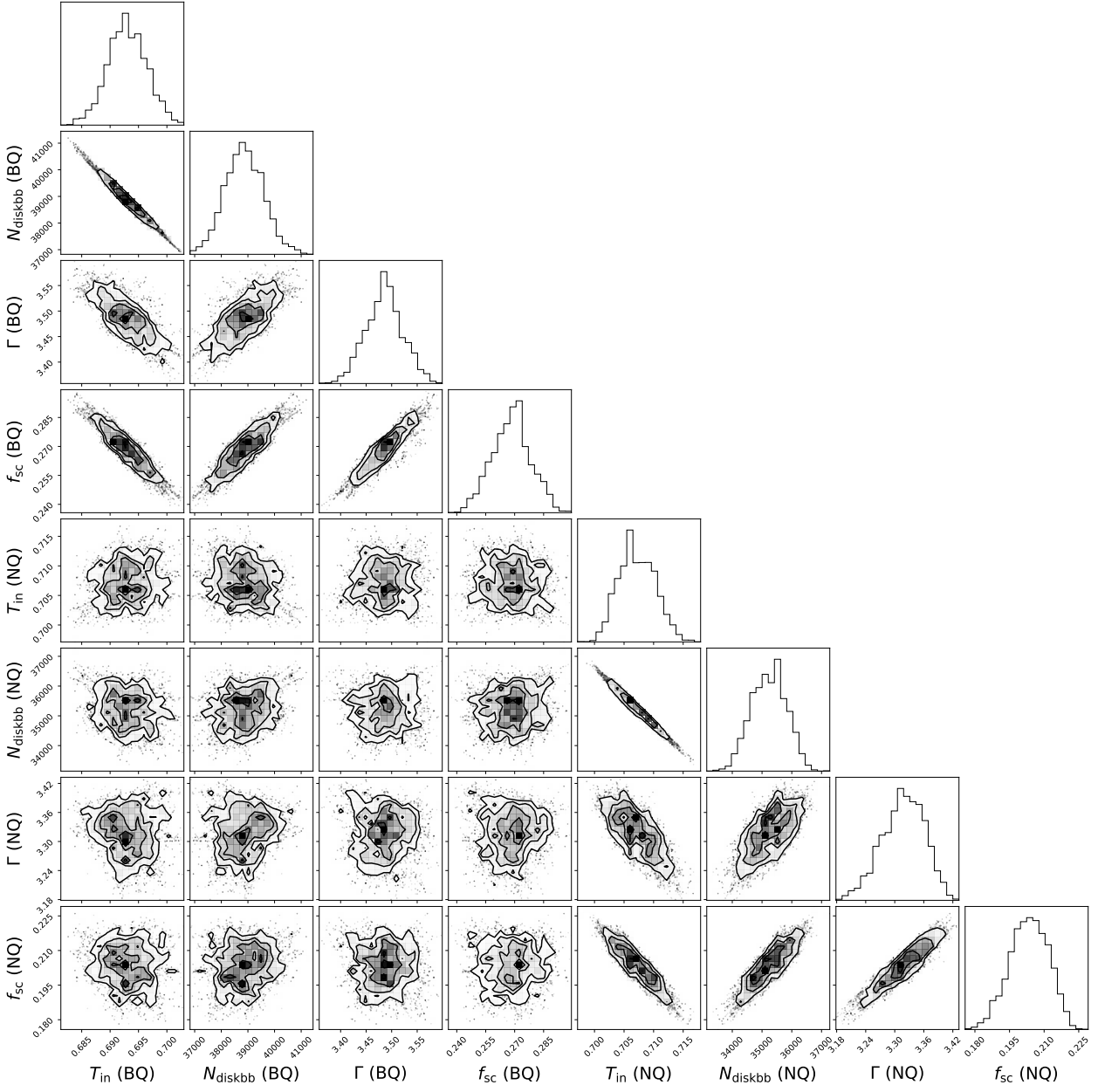
Figure A2. Distributions of the main best-fitting spectral parameters fitted with model 2: TBNEW*(DISKBB+NTHCOMP+GAUSSIAN) for Obs. #1: 1200530110.
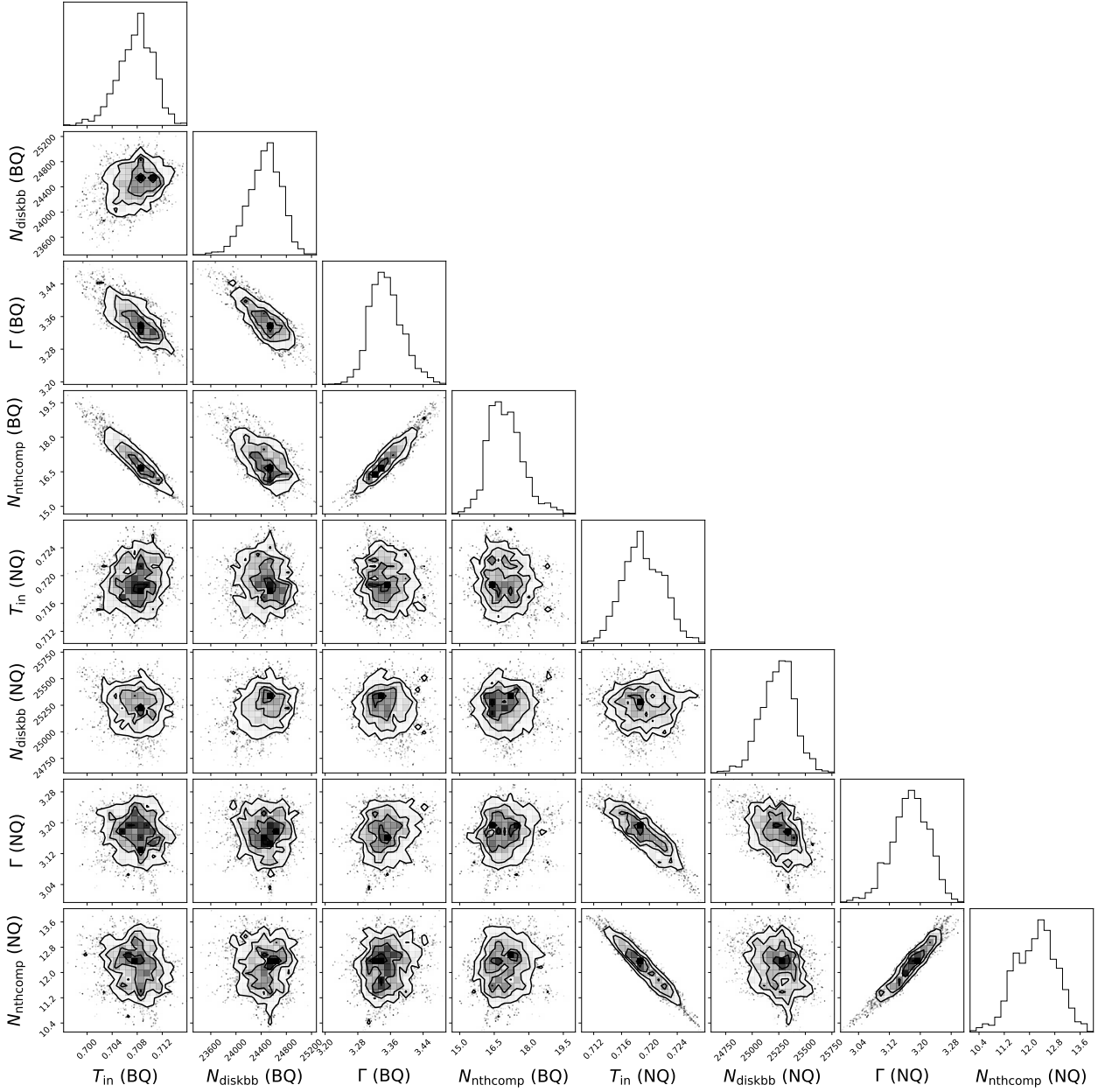
Table A1. Best-fitting spectral parameters for models 1 and 2. The spectra were extracted from all the orbits with and without the type-B QPO, respectively.

Component	Parameters	1200530110		1200530113		1200530117		1200530125	
		type-B QPO	non-QPO	type-B QPO	non-QPO	type-B QPO	non-QPO	type-B QPO	non-QPO
		Model 1: TBNEW*(SIMPL*DISKBB+GAUSSIAN)							
TBNEW	$N_{\rm H}$ ($\times 10^{22}$ cm^{-2})	0.89 ± 0.01		0.89 ± 0.01		0.89 ± 0.01		0.89 ± 0.01	
DISKBB	$kT_{\rm in}$ (keV)	0.691 ± 0.003	0.704 ± 0.003	0.671 ± 0.005	0.694 ± 0.005	0.657 ± 0.004	0.678 ± 0.003	0.636 ± 0.003	0.649 ± 0.003
	Norm	43272 ± 767	41662 ± 650	44946 ± 1166	41390 ± 977	44877 ± 901	41617 ± 688	43608 ± 800	41943 ± 688
SIMPL	Γ	3.45 ± 0.03	3.36 ± 0.03	3.33 ± 0.05	3.46 ± 0.07	3.36 ± 0.04	3.44 ± 0.07	3.34 ± 0.03	3.26 ± 0.03
	$f_{\rm SC}$	0.27 ± 0.01	0.22 ± 0.01	0.32 ± 0.02	0.23 ± 0.02	0.30 ± 0.01	0.16 ± 0.01	0.27 ± 0.01	0.20 ± 0.01
GAUSSIAN	$E_{\rm line}$ (keV)	6.4^a	6.4^a	6.4^a	6.4^a	6.4^a	6.4^a	6.45 ± 0.07	6.40 ± 0.06
	σ (keV)	0.70 ± 0.09	0.63 ± 0.06	0.5^a	0.5^a	0.5^a	0.5^a	0.52 ± 0.07	0.61 ± 0.07
	Norm	0.028 ± 0.005	0.031 ± 0.004	0.012 ± 0.005	0.024 ± 0.005	0.012 ± 0.003	0.016 ± 0.003	0.018 ± 0.003	0.021 ± 0.003
	χ^2/dof	440.8/447		456.6/447		427.4/449		452.0/445	
		Model 2: TBNEW*(DISKBB+NTHCOMP+GAUSSIAN)							
TBNEW	$N_{\rm H}$ ($\times 10^{22}$ cm^{-2})	0.90 ± 0.01		0.89 ± 0.01		0.90 ± 0.01		0.89 ± 0.01	
DISKBB	$kT_{\rm in}$ (keV)	0.705 ± 0.003	0.715 ± 0.003	0.688 ± 0.004	0.706 ± 0.004	0.671 ± 0.003	0.684 ± 0.003	0.649 ± 0.003	0.658 ± 0.003
	Norm	27324 ± 200	29156 ± 165	25458 ± 385	28121 ± 374	26662 ± 268	32433 ± 239	27459 ± 189	30104 ± 185
NTHCOMP	Γ	3.33 ± 0.03	3.24 ± 0.03	3.22 ± 0.05	3.33 ± 0.07	3.25 ± 0.03	3.32 ± 0.06	3.23 ± 0.03	3.16 ± 0.03
	Norm	18.9 ± 0.7	15.6 ± 0.6	21.0 ± 1.1	15.8 ± 1.1	18.4 ± 0.7	10.2 ± 0.6	14.7 ± 0.5	11.4 ± 0.5
GAUSSIAN	$E_{\rm line}$ (keV)	6.4^a	6.4^a	6.4^a	6.4^a	6.4^a	6.4^a	6.42 ± 0.07	6.37 ± 0.06
	σ (keV)	0.73 ± 0.09	0.65 ± 0.06	0.5^a	0.5^a	0.5^a	0.5^a	0.56 ± 0.08	0.63 ± 0.07
	Norm	0.031 ± 0.005	0.032 ± 0.004	0.013 ± 0.005	0.025 ± 0.005	0.013 ± 0.003	0.016 ± 0.003	0.020 ± 0.004	0.022 ± 0.004
	χ^2/dof	447.0/447		458.9/447		432.1/449		457.8/445	
	$F_{\rm diskbb}{}^b$	11.41	12.88	9.55	11.77	8.99	11.88	7.96	9.26
	$F_{\rm nthcomp}{}^b$	8.53	7.27	9.53	7.15	8.09	4.50	6.31	5.06
	$F_{\rm gaussian}{}^b$	0.03	0.03	0.01	0.03	0.01	0.02	0.02	0.02
	$F_{\rm total}{}^b$	19.97	20.18	19.09	18.95	17.09	16.40	14.29	14.34

[a] Fixed.

[b] 0.6–10 keV unabsorbed flux in units of 10^{-8} erg cm^{-2} s^{-1}.

Table A2. Best-fitting spectral parameters for model: TBNEW*(SIMPL*DISKBB+CONSTANT*DISKBB+GAUSSIAN). The spectra of the period with and without the type-B QPO were extracted from one or two single orbits before and after the transition.

Component	Parameters	1200530110		1200530113		1200530117		1200530125	
		type-B QPO orbit 4	non-QPO orbit 3	type-B QPO orbit 2&3	non-QPO orbit 4	type-B QPO orbit 5	non-QPO orbit 4	type-B QPO orbit 5	non-QPO orbit 6&7
		Model: TBNEW*(SIMPL*DISKBB+CONSTANT*DISKBB+GAUSSIAN)							
TBNEW	$N_{\rm H}$ ($\times 10^{22}$ cm^{-2})	0.89 ± 0.01		0.89 ± 0.01		0.89 ± 0.01		0.89 ± 0.01	
DISKBB	$kT_{\rm in}$ (keV)	0.693 ± 0.004	0.708 ± 0.004	0.671 ± 0.006	0.694 ± 0.005	0.651 ± 0.005	0.678 ± 0.005	0.640 ± 0.004	0.645 ± 0.003
	Norm	11624 ± 739	8234 ± 574	14758 ± 1418	9480 ± 872	15153 ± 1212	8812 ± 1036	10981 ± 796	9187 ± 495
SIMPL	Γ	3.48 ± 0.04	3.30 ± 0.05	3.37 ± 0.06	3.46 ± 0.08	3.46 ± 0.05	3.36 ± 0.10	3.35 ± 0.05	3.27 ± 0.04
CONSTANT	effective $f_{\rm SC}$	0.27 ± 0.01	0.20 ± 0.01	0.33 ± 0.02	0.23 ± 0.02	0.33 ± 0.02	0.21 ± 0.02	0.26 ± 0.01	0.22 ± 0.01
GAUSSIAN	$E_{\rm line}$ (keV)	6.4^a	6.4^a	6.4^a	6.4^a	6.4^a	6.4^a	6.42 ± 0.13	6.48 ± 0.08
	σ (keV)	0.56 ± 0.10	0.62 ± 0.12	0.5^a	0.5^a	0.5^a	0.5^a	0.57 ± 0.13	0.49 ± 0.09
	Norm	0.024 ± 0.006	0.030 ± 0.007	0.017 ± 0.006	0.024 ± 0.005	0.016 ± 0.004	0.023 ± 0.006	0.021 ± 0.006	0.018 ± 0.004
	χ^2/dof	$422.2/447$		$462.9/445$		$461.9/436$		$457.6/445$	

^{a} Fixed.
^{b} 0.6–10 keV unabsorbed flux in units of 10^{-8} erg cm^{-2} s^{-1}.

This paper has been typeset from a TEX/LATEX file prepared by the author.